LANGMUIR

pubs.acs.org/Langmuir Article

Monolayer-Protected Gold Nanoparticles Functionalized with Halogen Bonding Capability—An Avenue for Molecular Detection Schemes

Quang Minh Dang, Samuel T. Gilmore, Karthik Lalwani, Richard J. Conk, Jeffrey H. Simpson, and Michael C. Leopold*

Cite This: https://doi.org/10.1021/acs.langmuir.2c00381 Read Online

ACCESS | Metrics & More | Article Recommendations | Supporting Information

ABSTRACT: The use of functionalized nanoparticles (NPs) and their aggregation in the presence of a targeted analyte is a well-established molecular detection strategy predicated on harnessing specific molecular interactions to the NP periphery. Molecules able to specifically interact with the functionalized NPs alter the unique optical and electrochemical properties of the NPs as a function of interparticle spacing. While many intermolecular interactions have been successfully exploited in this manner in conjunction with aqueous NP systems, the use of non-aqueous NPs in the same capacity is significantly less explored. A fundamental interaction that has not been previously investigated in NP schemes is halogen bonding (XB). XB is an orthogonal, electrostatic interaction between a region of positive electrostatic potential ($\delta+$) on a halogen atom (i.e., XB donor) and a negative ($\delta-$) Lewis base (XB acceptor) molecule. To couple XB with NP systems, ligands featuring a molecular structure that promotes XB interactions need to be identified, optimized, and synthesized for subsequent attachment to NPs. Herein, density functional theory (DFT) and NMR techniques are used to identify a strong XB-donor moiety ($-C_6F_4I$) and a synthetic scheme for a thiolate ligand featuring that functionality is devised and executed with high purity/yield (78%). Ligand-exchange reactions allow functionalization of non-aqueous alkanethiolate-protected gold NPs or monolayer-protected clusters (MPCs) with the XB-donor ligands. Functionalized MPCs (f-MPCs), within both assembled films and in solution, are shown to engage in XB interactions with target XB-acceptor molecules. Molecular recognition events, including induced aggregation of the f-MPCs, are characterized with UV−vis spectroscopy, cyclic voltammetry, TEM imaging, and diffusion-ordered spectroscopy NMR with limits of detection of 50−100 nM for strong XB acceptors. While fundamental exploration of XB interactions is ongoing, this study represents a step toward utilizing XB within molecular detection schemes, an application with implications for supramolecular chemistry, forensic, and environmental chemical sensing.

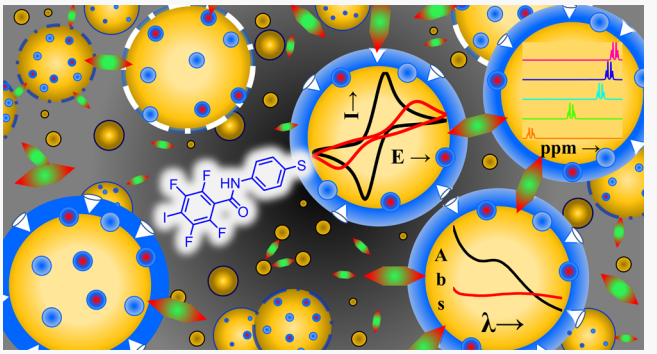

1. INTRODUCTION

The use of colloidal metallic nanoparticles (NPs) offers the unique optical property of localized surface plasmon resonance—a well-established strategy in the development of solution-based molecular detection schemes, many examples of which are summarized in well-organized review articles.[1−5] Surface plasmon resonance refers to the specific phenomenon of metallic NPs in which the oscillation frequency of their collective surface electrons can match that of the incident light and allow metallic NPs to absorb the energy of incident light to produce a broad absorption in the visible region of the electromagnetic spectrum known as the surface plasmon band (SPB).[3] Over the years, research has established that the SPB intensity and location (λ_{max}) are sensitive to specific features of the NP system, including their core size and interparticle spacing,[6] core composition,[7] and changes to NP surface properties such as the dielectric medium upon NP modification.[8,9] As such, the establishment and monitoring of the NP's SPB properties in solution have become routine for characterizing the synthesized NPs' properties as well as their chemical modification. Moreover, the dependence of the SPB on the inter-particle spacing of NPs has become the foundation of studying functionalized colloidal NPs as part of aggregation-based molecular recognition schemes.[1] In such systems, the addition of targeted analyte molecules to NP solutions induced significantly decreased spacing between individual NPs (i.e.,

Received: February 14, 2022
Revised: March 24, 2022

forming NP aggregates) that subsequently resulted in the reduction, elimination, or red shift of the SPB compared to the original well-spaced, independent NPs in the absence of the analyte. This well-established approach remains of interest to the scientific community because of its simplicity and relatively low cost and because the detection can often be observed visually or with a simple spectrophotometer.[1]

Literature reports on NP aggregation-based molecular detection schemes are dominated with the study of aqueous gold NP (Au-NP) systems typically involving either silver[10] or gold cores whose surfaces are modified with various ligands such as citrate,[11−15] tiopronin,[16] thioctic acid,[17] and mercaptobenzoic acid.[18,19] In addition, aqueous systems of this nature are inherently attractive because the NPs feature strong SPB absorption, which is characteristic of well-spaced, independent NPs in solution, which shifts dramatically upon an aggregation event instigated by the presence of a molecule that is able to interact with two or more NPs. For these systems, the aggregation event is often colorimetric: red shifts of the SPB to longer wavelengths upon aggregation manifest as visible solution color changes (e.g., wine red to gray/blue or from pale yellow to brown for Au-NP and Ag-NP systems, respectively).[1] In addition to being colorimetric, the aggregation events are also easily characterized with UV−vis spectroscopy where decreases and shifts of the SPB are systematic over time. Aggregation can be further visualized by transmission electron microscopy with imaging that often shows dramatic changes in interparticle spacing, particle agglomeration, and, at a high enough analyte concentration, eventual NP aggregation. Despite the prevalence of these aqueous NP systems in the literature, analogous reports of analyte-induced NP aggregation for *non-aqueous* NP systems are comparatively underrepresented. In particular, reports of NP aggregation-based molecular recognition systems using alkanethiolate-protected Au-NPs, often referred to as monolayer-protected clusters (MPCs),[20−22] are exceedingly rare.[19] Alkanethiolate MPCs are more typically used to form NP films at surfaces via electrostatic or covalent interactions, and the SPB reflects both core size and spacing within the films.[6,23,24] While the existing NP aggregation schemes cover a wide range of water-soluble target molecules, the extension of the strategy to more non-polar targets would broaden the range of application and complement the existing aqueous methods by providing a tool for less polar molecules of interest (see below).

NP-based aggregation schemes have been used as colorimetric assays targeting a range of biomedical, environmental, forensic, and food-related analytes.[1,25] The examples include detection of cancer biomarkers (e.g., sialic acid),[14] pesticides (e.g., chlorothalonil),[13] antibiotics (e.g., ofloxacin),[11] toxic or disease-related metal cations (e.g., Ag^{1+}, Al^{3+}, and Hg^{2+}),[10,15,26] physiologically relevant cations (e.g., K^{1+}),[27,28] narcotics (e.g., codeine),[29] explosives (e.g., trinitrotoluene, TNT),[25,30,31] and steroids (e.g., progesterone).[12] Additionally, a number of reports have explored using NP aggregation events for DNA detection.[32] In nearly all cases, the approach offers analytical effectiveness (sensitivity and selectivity), simplicity, and low cost and usually requires no complex instrumentation.[1] The major prerequisite of these NP schemes is consistently the ability to engineer functionalized NPs that are independent in solution until a specific interaction with targeted analyte molecules induces their aggregation.

Over the years, a number of specific molecular interactions between functionalized NPs and targeted analytes have been employed in NP aggregation schemes, including hydrogen bonding, electrostatic, donor−acceptor, van der Waals, and ion complexation/chelation interactions. The general strategy in most of these studies is to synthesize aqueous citrate-stabilized gold NPs (CS-NPs) and subsequently functionalize them via place-exchange reactions to harness a specific interaction to the NP periphery. For context, reports by Mao et al.,[30] Liu et al.,[25] and Ray et al.[31] each modified CS-NPs with cysteamine, ethylene diamine, and aminothiophenol, respectively, to employ donor−acceptor chemistry that induced NP aggregation events in the presence of picomolar TNT. Ai and co-workers utilized the three-point hydrogen bonding interactions between thiol-functionalized cyanuric acid derivative-stabilized CS-NPs and melamine, an illegal additive to milk and infant formula.[33] Chen et al.[27,28] modified citrate and thioctic acid NPs with 15-crown-5-substituted alkanethiols, which showed aggregation with striking color changes in the presence of potassium ions through chelation. Similarly, chelation-induced aggregation of CS-NPs functionalized with mercaptopropionic acid and homocysteine was used by Chandra Ray et al. to detect Hg^{2+} at 5 ppb limit of detection.[34] More recently, in 2018, Feng et al. employed unfunctionalized CS-NPs to detect the pesticide chlorthalonil,[13] while Rujiralai et al. modified CS-NPs with aminophenylboronic acid to detect sialic acid, a biomarker for cancer, in simulated saliva.[14] Both of these studies utilized analyte disruption of the existing electrostatic NP interactions to induce colorimetric aggregation. In 2018, Lahtinen and co-workers reported the formation of gold nanocluster oligomers with the addition of biphenyldithiol ligands to solutions of *p*-mercaptobenzoic acid-protected Au-NPs.[19] As previously mentioned, literature examples of NP aggregation systems utilizing non-aqueous, alkanethiolate-protected MPCs were exceedingly rare.

In all these literature reports, NP aggregation is initiated via a specific interaction that the NPs have been purposely functionalized with to engage with analyte molecules. To our knowledge, the employment of a more recently established intermolecular interaction called halogen bonding (XB) in this capacity is absent from the scientific literature. XB is a highly directional, non-covalent, and electrostatic interaction between a region of positive electrostatic potential on a halogen atom (XB donor) and a Lewis base (XB acceptor).[35] The region of positive electrostatic potential, also known as the "sigma (σ) hole", on the XB donor is created as electronegative groups bonded to a polarizable halogen atom pull e^- density from the halogen atom along the σ bond axis. XB is more directionally constrained than hydrogen bonding due to the σ-hole forming along the covalent bond of the halogen atom. The size of the σ-hole is tunable with variations in the halogen atom's polarizability and electronegativity as well as the strength of the e^- withdrawing groups (EWGs) associated with the halogen atom.[35−37] While XB has been explored computationally in small inorganic and organic molecular systems[38] as well as within DNA base pairing,[39] experimental application of XB, particularly in combination with computational support, appears less often in the literature. The most relevant experimental reports, such as those from the van der Boom group, employed XB interactions to perform step-wise assembly of Au-NP films at planar surfaces[40,41]—work suggesting that such XB interaction may be strong enough to induce NP aggregation.

https://doi.org/10.1021/acs.langmuir.2c00381
Langmuir XXXX, XXX, XXX−XXX

Scheme 1. Synthesis Scheme for the XB-Donor Thiolate Ligand (2,3,5,6-Tetrafluoro-4-iodo-*N*-(4-mercaptophenyl)benzamide—[5])

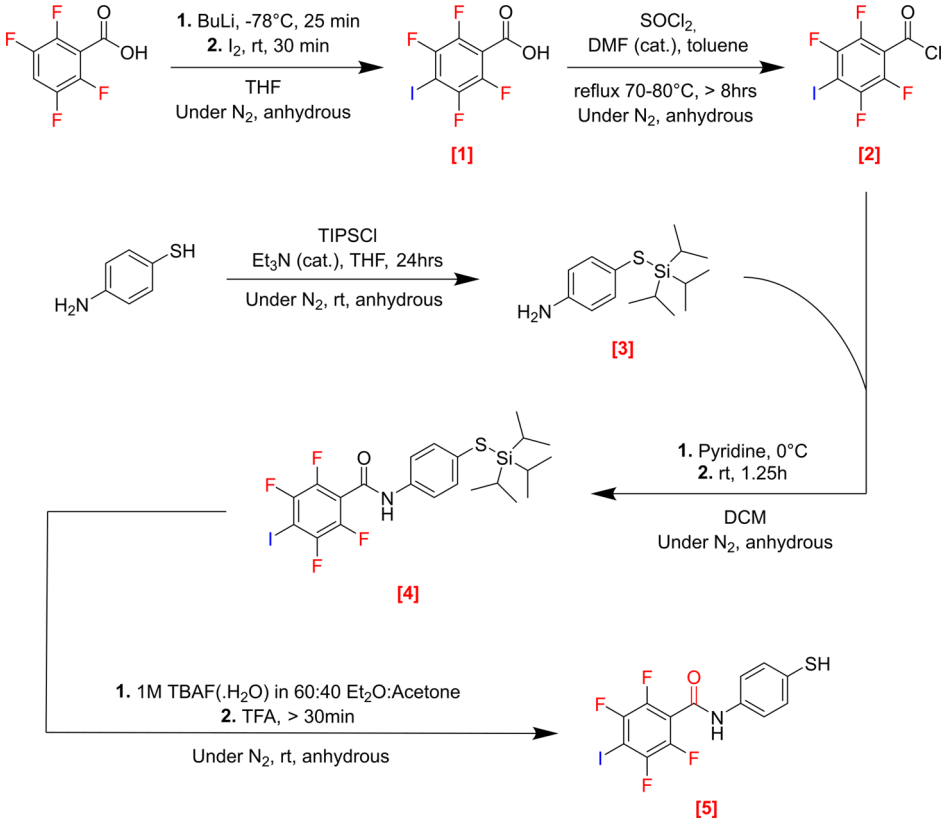

In this paper, a molecular detection scheme based on the aggregation of non-aqueous, alkanethiolate-protected Au-NPs or Au-MPCs, which are specifically functionalized with a unique ligand to engage in XB interactions, is presented. This work builds on our prior reports investigating XB and the optimal molecular structure that will promote strong XB interactions.[42,43] While it is well established that structures featuring a halogen surrounded by EWGs allow for the formation of a σ-hole on the halogen that can subsequently engage in XB interactions to varying degrees,[44] our prior experimental and computational studies showed that halogen-substituted arenes can function well as XB donors that are able to interact with XB-acceptor molecules both in the gas phase and in solution.[42,43] More specifically, our 2019 study showed, both computationally and experimentally, effective XB interactions using 1,4-dihalotetrafluorobenzene molecules as XB donors.[42] Similarly, a study from our group in 2021 combining density functional theory (DFT) computations, ^{1}H and ^{19}F NMR measurements, and ^{1}H−^{19}F HOESY NMR established strong XB interactions in solution between 1-halopentafluorobenzene molecules as XB donors and a range of XB-acceptor molecules.[43] Those prior studies inform the current study, which synthesizes and utilizes a 4-iodoperfluorophenyl thiolate ligand with XB-donor capability for Au-MPC modification and subsequently harnesses the XB-donor capability and the unique properties of NPs to develop XB-based molecular detection schemes. Using computational tools in conjunction with spectroscopic methods, electrochemistry, and microscopy characterization, an experimental scheme is systematically designed and developed, including a challenging synthesis of an XB-donor thiolate ligand that is able to promote XB interactions between functionalized MPCs (f-MPCs). To our knowledge, this is the only study utilizing these materials for this purpose and successfully establishing XB-induced aggregation of NPs that signal the presence of molecules. More specifically, a number of literature reports have already identified XB interactions among classes of compound that would be desirable to detect via NP aggregation, including certain rare explosives (e.g., cyclotrimethylene trinitramine or RDX) for counter-terrorism,[42,45,46] insecticides (e.g., neonicotinoids) harmful to the environment,[47,48] certain narcotics (e.g., opioids),[49] as well as biomedical targets.[50]

2. EXPERIMENTAL SECTION

2.1. Materials and Instrumentation. All chemicals were purchased commercially (Millipore-Sigma, Oakwood Chemical, Fisher Scientific, TCI, and Strem Chemicals) and used without further purifications or modifications. All aqueous solutions and/or reactions were prepared or conducted with 18.02 MΩ·cm ultrapurified water. Bruker Avance III 400 MHz and Bruker Avance I 500 MHz NMR spectrometers were used throughout the study with chemical shifts reported relative to tetramethylsilane (TMS) and trichlorofluoromethane ($CFCl_3$) for ^{1}H and ^{19}F NMR, respectively. NMR spectra were analyzed using Mestrelab's MestreNova (v14.2). Mass spectrometry data was collected on a Shimadzu LCMS-IT-TOF high-resolution spectrometer. Infrared spectra were collected on a FTIR spectrometer (Thermo Scientific, Nicolet iS10). An Agilent 8453 ultraviolet−visible photodiode array spectrophotometer was used to characterize the surface plasmon resonance of Au-NPs in solution and their XB-induced aggregation. Transmission electron microscopy (JEOL 1010 with Advanced Microscopy Techniques XR-100 CCD image collection operating at 80−100 kV) analysis was used to quantify Au-NP diameter and characterize XB-induced Au-NP

https://doi.org/10.1021/acs.langmuir.2c00381
Langmuir XXXX, XXX, XXX−XXX

aggregation by drop-casting 5 μL samples in toluene onto 400 mesh Formvar-coated copper grids (Electron Microscopy Sciences). Before further analysis, each grid was imaged in ≥5 different areas to ensure that imaging was representative of the surface characteristic. The diameters of the functionalized MPCs were then measured by pixel by standardizing the scale bar of the microscopy image using Adobe Photoshop for at least 100 nanoparticles per sample. Cyclic voltammetry was performed by CH Instruments potentiostats (650A and 610B) in electrochemical sandwich cells previously demonstrated by our laboratory[51] and that feature an Ag/AgCl (saturated KCl) reference electrode (Microelectrodes, Inc), a platinum wire (Sigma-Aldrich) counter electrode, and an evaporated gold substrate (EMF Corp., Ithaca, NY) as a working electrode defined by a Viton O-ring (0.32 cm^2).

2.2. Computational Analysis. Halogen bonding is difficult to characterize since the interaction encompasses dispersion, electrostatic, and charge-transfer effects. As in our prior report,[43] DFT employing M06-2X/cc-pVTZ//M06-2X/cc-pVDZ was used to estimate optimal gas-phase geometries and energy of interaction for XB molecular adducts. Calculations were conducted using the Gaussian16 software[52] with the M06 functional[53] and the cc-pVDZ[54] (geometry optimization) and cc-pVTZ[55] (single point) basis sets to estimate several parameters of XB adducts: energy of interaction (ΔE_{int}) or binding energy, XB bond lengths (X−B), and XB bond angles (R−X−B). It should be noted that, in this study, relative comparisons and not absolute energetic evaluations were targeted during computational analysis. In general, strong XB interactions are typically characterized by bond lengths shorter than the van der Waals distances of the interacting atoms and nearly linear (180°) R−X−B bond angles.[38,39,43,56,57] All optimized geometries of XB adducts were visualized using the GaussView program.[58] Additional experimental details of computational measurements for this study are included in the Supporting Information (p. S3).

2.3. NMR Spectroscopy. NMR spectroscopy was used in multiple ways during this study. In addition to its use as a traditional structural confirmation tool for ligand synthesis, NMR spectroscopy was employed in this study to measure the diffusion coefficients (D) of analytes and solvent molecules [diffusion-ordered spectroscopy (DOSY) NMR], the association constants (K_a) of XB adducts via NMR titrations, and to confirm the functionalization of Au-NPs with XB-donor ligand molecules. In all cases, as previously reported,[43,59] careful sample preparation was critical to useful NMR measurements. Experimental details of conducting both ^{19}F (376.46 MHz) and ^{1}H (400.13 MHz) NMR titrations at a fixed temperature (298 K) to determine association constants (K_a) for XB adducts have been previously published[43] and are also described in detail herein (Supporting Information, pp. S4−S5). In brief, a titration involved measurement of at least nine sequential samples in which the concentration of the XB donor was kept constant in the range of 0.0475−0.0525 M, depending on the XB donor−acceptor-solvent system, while the concentration of the XB acceptor was systematically increased from 0.0 M up to 5.0 M or until at least 50% host saturation was achieved.[43,60,61] As in prior studies, the chemical shifts of the XB donor changed with increasing concentrations of the XB acceptor. These chemical shifts were plotted as a function of XB acceptor concentration to yield binding isotherms as previously demonstrated in the literature.[43,44,60−62] Non-linear regression analyses with an in-house designed Python code[43] yielded relevant equilibrium association constants (K_a), a representation of XB strength for the respective XB adduct systems. DOSY NMR experimental parameters are provided in the Supporting Information (p. S3).

2.5. Thiolate XB-Donor Ligand Synthesis. The novel synthetic procedure for the XB-donor ligand was designed from the combined works of Biot and Bonifazi,[63] Hosoya and co-workers,[64] and Kunkle and colleagues[65] and executed successfully to synthesize a biphenyl amide-linked thiolate ligand featuring a strong XB-donor moiety (−C_6F_4I). The steps of the procedure are described below; the molecule numbers correspond to Scheme 1. Structural characterization (NMR and IR spectra) of the intermediates and the final product are provided in the Supporting Information (Figures S1−S10).

2.5.1. 2,3,5,6-Tetrafluoro-6-iodobenzoic Acid [1]. The following procedure was adapted from Biot and Bonifazi (2020).[63] To a 250 mL Schlenk flask was added 2,3,5,6-tetrafluorobenzoic acid (1.940 g, 10 mmol) and 160 mL of THF. The mix was degassed with N_2 and cooled to −76 °C. To the mixture, 11 mL of 2.3 M *n*-BuLi in hexanes was added dropwise. To the resulting pale-yellow mixture was then added dropwise I_2 (3.172 g, 12.5 mmol) dissolved in a minimal amount of THF. The resulting red mixture was allowed to warm to rt, at which time it became transparent. The mix was then diluted with 200 mL of 1:2 (v/v) aqueous sulfuric acid. The organic layer was removed from the resulting mixture, and the aqueous layer was extracted 3× with 20 mL of ether (60 mL total) before the organic layers were combined and further extracted 3× with 50 mL of water (150 mL total), 2× with 25 mL of saturated $Na_2S_2O_3$ (50 mL total), 1× with 50 mL of water, and finally 1× with 50 mL of brine. The resulting clear organic layer was then dried over anhydrous $MgSO_4$ and dried in vacuo to yield an off-white solid. Yield: **2.849 g (89%)**. ^{1}H NMR (400 MHz, $CDCl_3$): δ 9.47 (s, 1H). ^{19}F NMR (376 MHz, $CDCl_3$) δ −119.39 (m, 2F), −137.26 (m, 2F). HRMS (IT-TOF) m/z [M + CF_3COO^-]: calcd, 432.8813; found, 432.8808.

2.5.2. 2,3,5,6-Tetrafluoro-4-iodo-benzoyl Chloride [2]. The following procedure was adapted from Biot and Bonifazi.[63] To a 25 mL round-bottom flask (RBF) was added **1** (0.750 g, 2.34 mmol) and 1.5 mL of toluene. The resulting suspension was degassed under N_2, and to it was then added thionyl chloride (0.85 mL, 11.65 mmol) and three drops of DMF. The mixture was then refluxed overnight and allowed to cool to rt. The solvent was then removed from the mixture in vacuo, after which an additional 5 mL of toluene was added to the resulting oil and removed in vacuo. This process was repeated twice more to remove residual thionyl chloride. The resulting yellow oil was then used without further purification. **Yield: 0.736 g (93%)**. ^{19}F NMR (376 MHz, $CDCl_3$) δ −119.28 (m, 2F), −138.48 (m, 2F).

2.5.3. 4-[(Triisopropylsilyl)thio]benzenamine [3]. The following procedure was adapted from Hosoya and co-workers.[64] To a 25 mL RBF was added 4-aminothiophenol (2.00 g, 16.0 mmol) and 16 mL of THF. The resulting yellow solution was degassed over N_2. To the mixture was then added triethylamine (2.67 mL, 19.2 mmol), followed by triisopropylsilyl chloride (3.77 mL, 17.6 mmol) dropwise. A heavy suspension was then observed, which was allowed to stir at room temperature overnight. The solvent was then removed from the mixture in vacuo to obtain a crude yellow product. The product was then purified by flash chromatography on silica gel with a 50:50 ethyl acetate/hexanes mobile phase. The first eluent (R_f = 0.74) was identified as a product and collected as a pale-yellow oil. Yield: **4.144 g (92%)**. ^{1}H NMR (400 MHz, $CDCl_3$): δ 7.27 (d, J = 8.7 Hz, 2H), 6.58 (d, J = 8.7 Hz, 2H), 3.26 (s, 2H), 1.24 (hept, 7.2 Hz, 3H), 1.09 (d, J = 7.2 Hz, 18H). ^{13}C NMR (101 MHz, $CDCl_3$): δ 136.46, 115.70, 18.46, 17.72, 12.93, 12.31. **Yield: 4.354 g (97%)**. HRMS (IT-TOF): m/z [M + Na^+] calcd, 606.0377; found, 605.9916.

2.5.4. 2,3,5,6-Tetrafluoro-4-iodo-N-(4-[(triisopropylsilyl)thio]-phenyl)benzamide [4]. The following procedure was adapted from Kunkle and co-workers.[65] To a round-bottom flask was added 999 mg (3.55 mmol, 1.2 equiv) of [**3**] and 3 mL of DCM. The solution was then placed under a N_2 atmosphere and cooled to 0 °C, and 0.262 mL of pyridine (3.55 mmol, 1.2 equiv) was added dropwise. A solution was then prepared separately by combining 1.0 g (2.96 mmol, 1.0 equiv) [**2**] and 3 mL of DCM. This solution was then cooled to 0 °C and added dropwise to the RBF. The mixture was then allowed to warm to room temperature and stirred for 30 min. The resulting red solution was then concentrated under vacuum and purified by flash column chromatography (80:20 hexanes/ethyl acetate, R_f = 0.56) to yield the product as an off-white solid. Yield: **1.45 g (84%)**. ^{1}H NMR (400 MHz, $CDCl_3$): δ 8.01 (s, 1H), 7.48 (m, 4H), 1.27 (m, 3H), 1.11 (d, J = 7.3 Hz, 18H). ^{19}F NMR (376 MHz, $CDCl_3$): δ −119.11 (m, 2F), −140.17 (m, 2F). HRMS (ESI, IT-TOF): $[M]^+$ calcd, 584.0558; found, 584.0575.

2.5.5. 2,3,5,6-Tetrafluoro-4-iodo-N-(4-mercaptophenyl)-benzamide [5]. To a RBF, 925 mg (1.59 mmol, 1.0 equiv) of [**4**]

https://doi.org/10.1021/acs.langmuir.2c00381
Langmuir XXXX, XXX, XXX−XXX

was added with 2 mL ether. Under a N_2 atmosphere, a 1.0 M solution of TBAF in ether/acetone (1.75 mL, 1.1 equiv) was then added to the solution of [**4**] dropwise. The resulting slurry was then acidified with 0.133 mL of TFA (1.75 mmol, 1.1 equiv) resulting in a transparent solution. This was then concentrated under vacuum to obtain a yellow slurry, which was then washed several times with excess hexanes. The remaining solids were then dissolved in 20 mL of ether and extracted 5× with 10 mL of 0.1 M TFA buffer at pH = 1.6 (50 mL total). The organic phase was then dried over anhydrous $MgSO_4$ and concentrated under vacuum to yield the product as a white solid. Yield: **0.529 g (78%)**. ^{1}H NMR (400 MHz, DMSO-d_6): δ 10.92 (s, 1H), 7.55 (d, J = 8.6 Hz, 2H), 7.32 (d, J = 8.6 Hz, 2H), 5.44 (s, 1H). ^{19}F NMR (376 MHz, DMSO-d_6): δ −121.29 (m, 2F), −141.28 (m, 2F). HRMS (ESI, IT-TOF): $[M + Na]^+$ calcd, 449.9043; found, 449.8991.

2.6. Monolayer-Protected Cluster Gold Nanoparticle Synthesis. Hexanethiolate-protected monolayer-protected clusters (C6-MPCs) were synthesized from $HAuCl_4$ as described in previous literature using a modified Brust−Schiffrin procedure[66] involving a two-phase transfer. In brief, a typical preparation used an aqueous $HAuCl_4$ solution (3.39 g in 50.0 mL) mixed with a tetraoctylammonium bromide (4.25 g in 200 mL) toluene solution that is stirred for 1 h to transfer gold to the toluene layer. After discarding the aqueous layer, hexanethiol (2.0 mL) was added to the stirring toluene layer for 20 min before a solution of aqueous $NaBH_4$ (3.80 g in 20 mL) was added dropwise. With the addition of $NaBH_4$, a distinct darkening of the stirring solution was immediately observed as evidence of the formation of C6-MPCs. The mixture was stirred overnight at room temperature before being rotary-evaporated to near dryness and treated with reagent-grade acetonitrile (ACN) for overnight precipitation of C6-MPC. The mixture was filtered through a medium-fine glass frit, rinsed with copious amounts of ACN, dried, and collected for characterization (NMR, UV−vis, and TEM) as previously demonstrated (Supporting Information, Figures S11−S12). Consistent with prior reports, the *average* diameter of the C6-MPCs was measured to be 4.31 ± 0.08 nm, corresponding to an *average estimated* composition of $Au_{2951}(C6)_{876}$.[67]

2.7. Place-Exchange (Functionalization) of MPCs with a Synthesized Thiolate Ligand. C6-MPCs were functionalized with the synthesized thiolate XB-donor ligand (Scheme 1—[**5**]) to impart XB-donor capability via well-established place-exchange reactions.[68] Briefly, 200 mg of C6-MPC was co-dissolved in a RBF with 216 mg of the synthesized thiolate XB-donor ligand using 125 mL of anhydrous toluene. The mixture was stirred over the course of 5 days, during which a total of five incremental 25 mL aliquots were collected at different times (4 h, 1 day, 2 days, 3 days, and 5 days) and subsequently rotary-evaporated to dryness. As demonstrated in the literature, size exclusion chromatography (SEC) was employed to remove free thiolate XB-donor ligand molecules from each collected MPC aliquot.[69] Details of the SEC procedure are provided in the Supporting Information (pp. S19−S22). The success and relative degree of functionalization of each MPC aliquot with the XB-donor ligand was confirmed using a combination of iodine (I_2)-death reactions,[70] which cleave the Au−S bonds, and subsequent ^{19}F and ^{1}H NMR measurements, respectively, of the liberated disulfides. The degree of functionalization was determined via ^{1}H NMR measurements after I_2-death reactions by comparing the integrals of the XB-donor ligand's aromatic protons to those of the hexanethiol ligand's terminal methyl group to find their relative amount ratio. This ratio could then be converted to an average number of exchanged ligands based on established estimations of MPC compositions.[67] Additional details of this characterization, including ^{1}H NMR and ^{19}F NMR spectra of all functionalized MPC (f-MPC) aliquots before and after I_2 treatment, and the respective calculations of the extent of ligand exchange are presented in the Supporting Information (p. S23, Figure S16, and Table S1). The average composition of f-MPCs was estimated to be $Au_{2951}(C6)_{438}[\mathbf{5}]_{438}$.

2.8. Electrochemical Characterization of XB-Donor Capability of MPC Films. Self-assembled monolayers (SAMs) and MPC films were assembled on gold substrates using previously established procedures.[6,71] Briefly, gold substrates were mounted in electrochemical sandwich cells as working electrodes (described below) and electrochemically cleaned by cyclic voltammetry (0.1 M H_2SO_4 and 0.01 M KCl). Clean gold substrates were then exposed to an ethanol solution of 5 mM hexanethiol (C6-SH) overnight to form an initial SAM. SAM-modified gold was washed successively with EtOH and water prior to a 1 h treatment with a 5 mM ethanol solution of nonanedithiol (NDT), a linking ligand. After successive rinsing with EtOH, water, and toluene, the substrate was exposed to a ∼0.1 mg/mL solution (1 h; stirred with slowly bubbled N_2) of either functionalized (f-MPC) or unfunctionalized (control) C6-MPC (unf-MPC) in toluene. Successive exposure to NDT and MPC, known as a "dip cycle", was then repeated to form the MPC layer at the SAM-modified electrode. Each fully assembled MPC film was exposed for 1 h to a 1.0 mL solution of either 26 μM DABCO (1,4-diazabicyclo[2.2.2]octane), 26 μM Oct_3PO (trioctylphosphine oxide), 26 μM Bu_2CO (5-nonanone), or neat cyclohexane. Each step of film assembly was monitored electrochemically as described below.

Clean gold, SAM formation, and MPC film assembly could be systematically confirmed via measurement of non-Faradaic charging current at 120 mV during cyclic voltammetry (100 mV/s) from 0.1 to 0.4 V in a 0.25 M phosphate buffer solution (PBS) at each step of the process. Similarly, the cyclic voltammetry from −0.2 to +0.6 V (50 mV/s) of 5 mM potassium ferricyanide ($K_3Fe(CN)_6$) in an aqueous solution (0.5 M KCl), a redox probe, can be used to establish each step of the film formation as well by monitoring the qualitative changes in peak shape and quantitative changes in both peak current (i_p) and peak separation (ΔE_p). All potentials were measured versus the Ag/AgCl, satrd. KCl references. The same electrochemical techniques were also used to assess each film assembly's interaction with specific analyte and control molecules.

2.9. MPC Aggregation Experiments. XB-induced aggregation events of f-MPCs upon addition of XB-acceptor analytes were monitored and characterized by UV−vis spectroscopy and TEM imaging. For each sample, a 3.00 mL solution of f-MPCs in toluene with a concentration that yielded a SPB at 518 nm (herein referred to as A_{518}) of either 1.00, 0.50, or 0.20 a.u. was prepared in a dry, aqua regia-cleaned screw cap, special optical glass cuvette (Starna Cells). ***Caution:*** *Aqua regia, a 3:1 ratio of concentrated HCl/HNO$_3$, is extremely dangerous and should never be placed in a sealed container (appropriate PPE is required).* Stock solutions of XB-acceptor analytes in toluene were quantitatively prepared using an analytical balance and volumetric flask. A set volume of each analyte stock solution (1.0−10.0 μL) was drawn via a 10.0 μL microliter syringe (Hamilton Company) into a separate dry, aqua regia-cleaned screw cap, glass cuvette. The volume of each analyte stock solution was calculated to afford the final desired analyte concentration in a 3.00 mL solution. Each cuvette, along with the added volume of analyte stock solution, was placed under high-pressure vacuum for at least 1 h to remove the toluene solvent and yield the residual solid analyte. Subsequently, 3.00 mL solution of f-MPCs in toluene (A_{518} = 1.00, 0.50, or 0.20 a.u.) was transferred into the analyte-containing cuvette. UV−vis absorption spectra of the MPC samples were collected before and after the addition of analyte at 5 min and after 3 days.

3. Results and Discussion. *3.1. Assessment Tool for XB Interaction Strength (DOSY-NMR).* Prior work has identified effective XB-donor perfluorinated molecules of 1,4-diiodotetrafluorobenzene and iodopentafluorobenzene (IPFB) as able to engage in strong XB interactions both in gas and solution phases, respectively.[42,43] Fluorine EWGs are more optimal for XB because, unlike carbonyl or nitro EWGs, they lack the ability to engage in dipole−dipole or hydrogen bonding interactions—non-XB interactions that can lessen the strength and specificity of XB interactions between XB donor and XB acceptor molecules.[42,43] Prior studies of these interactions established DFT, NMR titration analysis, and 2-D HOESY NMR as feasible tools that can be used to assess for the XB strength of XB adducts.[43,72,73] One goal of the current study was to investigate an additional tool that can measure the diffusion coefficients of molecules in solution as an avenue to assess for XB interactions in

https://doi.org/10.1021/acs.langmuir.2c00381
Langmuir XXXX, XXX, XXX−XXX

solution: DOSY NMR. The hypothesis is straightforward in that freely diffusing molecules of significant size would diffuse faster than the same molecules engaging in significant intermolecular interactions, specifically XB interactions, with other molecules in solution. For this proof-of-concept DOSY NMR experiment, DABCO (1,4-diazabicyclo-2,2,2-octane) was selected as the XB acceptor analyzed in the presence and absence of IPFB (a strong XB donor); DABCO has been established as a strong XB acceptor.[60,73]

A set of eight DOSY NMR measurements on experimental and control systems were conducted with results summarized in Table 1.

Table 1. DOSY NMR Measurements of Diffusion Coefficients (D) for Various XB Donors with DABCO (100 mM)

#	XB donor	solvent	target	log D (log(m^2/s))
1	none	$CDCl_3$	residual $CHCl_3$	−8.49 (±0.02)
2	none	$CDCl_3$	^{1}H DABCO	−8.62 (±0.03)
3	none	toluene-d_8	^{1}H DABCO	−8.68 (±0.04)
4	IPFB (100 mM)	toluene-d_8	^{1}H DABCO	−8.77 (±0.04)
5	none	toluene-d_8	^{1}H toluene-d_7h_1	−8.59 (±0.02)
6	IPFB (100 mM)	toluene-d_8	^{1}H toluene-d_7h_1	−8.62 (±0.03)
7	perfluorotoluene (100 mM)	toluene-d_8	^{1}H DABCO	−8.64 (±0.13)
8	perfluorotoluene (100 mM)	toluene-d_8	^{1}H toluene-d_7h_1	−8.59 (±0.03)

For each system, the log D (diffusion coefficient) values, which represent the relative mobility of each molecule with a more negative value corresponding to slower mobility, of DABCO (analyte) and solvent molecules are measured. For following the discussion of these results, it is conducive to refer to the experiment numbers listed in the first column of Table 1. As an initial control (experiment **#1** and **#2**, Table 1), the log D values were measured for the residual $CHCl_3$ versus DABCO in $CDCl_3$ to verify the feasibility of the experimental methodology. The log D value of DABCO (−8.62), the bigger molecule, is significantly more negative than that of residual $CHCl_3$ (−8.49), which suggests that DABCO diffuses slower in solution than $CHCl_3$. Using the same technique, the log D values of DABCO, a strong XB acceptor, in the presence and absence of IPFB, a strong XB donor molecule that should form XB interactions with DABCO,[73] in toluene-d_8 were collected (experiment **#3** vs **#4**, Table 1). In this case, the log D values show a distinctly measurable decrease in the mobility of DABCO in the presence (log D = −8.77) of IPFB than in the absence of IPFB (log D = −8.68), suggesting the presence of XB interactions in the system. A number of internal controls were also conducted to establish that the measured change in mobility is most likely due to XB interactions. Experiments **#5** and **#6** (Table 1) compare log D values of toluene solvent molecules (toluene-d_7h_1) in both solutions of only DABCO and DABCO in the presence of IPFB, which show an insignificant difference in the log D values: −8.59 (±0.02) and −8.62 (±0.03), respectively. This result attributes the difference in the mobility of DABCO in the presence and absence of IPFB to an interaction between those two molecules rather than being impacted by solvent molecules. As a final control (experiments **#3** and **#4**, Table 1), additional evidence that DABCO's diminished mobility in the presence of IPFB could be attributed to XB interactions is obtained by measuring the log D value of DABCO in the presence of perfluorotoluene, a weak XB-donor molecule that lacks bromine or iodine halogen substitution required for strong XB interactions.[42,43] In this case, as expected, there is virtually no difference in the DABCO mobility when it is by itself (experiment **#3**, log D = −8.68) and in the presence of the perfluorotoluene (experiment **#7**, log D = −8.64). As previously observed, an internal check of the log D values of toluene solvent molecules (toluene-d_7h_1) (experiments **#5** vs **#8**) revealed no significant difference (log D = −8.59 (±0.02) vs −8.59 (±0.03), respectively). Taken collectively, these results suggest that DOSY NMR can serve as a complementary technique to assess XB interaction strength and as a tool to be utilized when differences in molecular mobility created by such intermolecular interactions are expected to be significant (see below).

3.2. XB Donor Strength as a Function of Fluorination Substitution. While aromatic XB donors such as IPFB offer great versatility in tuning the size of the σ-hole, a property shown to correspond to XB-donor strength,[42,43] the creation of a ligand for subsequent harnessing of the XB-donor moieties to Au-NPs would require the disruption of fluorine EWGs on the ring structure. As such, one goal of the research herein was to assess the impact of varying the patterns and locations of these fluorine aromatic substitutions on XB-donor strength. A set of five different iodoperfluorinated benzene structures as XB donors was studied: IPFB, 2,6-difluoroiodobenzene, 2,4,6-trifluoroiodobenzene, 3,4,5-trifluoroiodobenzene, and 2,3,5,6-tetrafluoroiodobenzene (Figure 1, *left*). The strength of XB interactions between these XB donors and an optimal XB-acceptor molecule, tributylphosphine oxide (Bu_3PO),[43,44] was assessed both computationally using DFT and experimentally with NMR titration analysis.

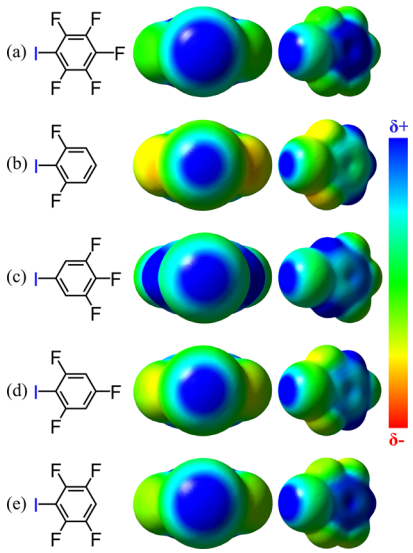

Figure 1. Electrostatic potential diagrams illustrating "σ-holes" of various fluorine ring substitutions of iodoperfluorophenyl XB donors, including (a) iodopentafluorobenzene, (b) 2,6-difluoroiodobenzene, (c) 3,4,5-trifluoroiodobenzene, (d) 2,4,6-trifluoroiodobenzene, and (e) 2,3,5,6-tetrafluoroiodobenzene.

Computational modeling and calculations of the interaction energies (ΔE_{int}), XB bond length/distance (XBD), and R−X−B bond angle (Θ) of the respective XB adducts were measured, with more negative ΔE_{int}, shorter XBD distances, and more linear Θs (approaching 180°) serving as indicators of stronger XB adducts.[42,43] Figure 1 (*right*) illustrates the electrostatic potential diagrams and the computationally measured sizes of the σ-hole for all the five XB donors as a function of their fluorine substitution patterns. The modeling suggests that the substantial positive electrostatic potential at the σ-hole can be maintained with different fluorine substitution patterns. Compared to IPFB (Figure 1a), any loss of fluorine substitution results in smaller σ-holes in XB donors. This decrease is most notable for the ortho-substituted fluorine XB donor (2,6-difluoroiodobenzene, Figure 1b), which exhibits a relatively small positive electrostatic potential despite maintaining EWGs nearest to the iodine atom (σ-hole). XB donors of 2,4,6-trifluoroiodobenzene (Figure 1c) and 3,4,5-trifluoroiodobenzene (Figure 1d) showed similarly diminished σ-holes. For our purposes, however, the most

https://doi.org/10.1021/acs.langmuir.2c00381
Langmuir XXXX, XXX, XXX−XXX

Table 2. Experimental K_a Values and M06-2X/cc-pVTZ//M06-2X/cc-pVDZ Interaction Energies (ΔE_{int}), Bond Distances (XBD), and Bond Angles of XB Adducts of XB Donors and XB Acceptor Bu_3PO

XB donors	ΔE_{int} (kcal/mol)[a]	X–B distance (Å)	R–X–B angle (θ)	K_a (M^{-1})[b]
iodopentafluorobenzene	−10.95	2.74	175.9	22.08 $(\pm 1.02)_{n=4}$
2,6-difluoroiodobenzene	−8.79	2.83	170.8	*2.91 (±0.11)*$_{n=3}$
3,4,5-trifluoroiodobenzene	−8.50	2.83	175.3	3.11 $(\pm 0.16)_{n=3}$
2,4,6-trifluoroiodobenzene	−9.16	2.81	171.4	4.72 $(\pm 0.16)_{n=3}$
2,3,5,6-tetrafluoroiodobenzene	−10.59	2.75	175.6	14.23 $(\pm 1.50)_{n=2}$
2,3,5,6-tetrafluoro-4-iodobenzamide	−11.17	2.73	175.7	[c]
2,3,5,6-tetrafluoro-4-iodo-*N*-(4-mercaptophenyl)benzamide	−11.67	2.72	175.9	[c]

[a] ΔE_{int} = E(XB adduct) − [E(XB donor) + E(XB acceptor)] (gas-phase values). [b] Determined from non-linear regression modeling of 1:1 binding isotherms collected during NMR titrations in cyclohexane. [c] No NMR titrations were performed. *Italicized K_a values* indicate non-plateauing binding isotherms as a result of non-specific (non-XB) intermolecular interactions. Computational interaction energies, bond distances, and bond angles of control adducts of all XB donors and hexane are included in the Supporting Information (Figure S19).

significant modeling was that of 2,3,5,6-tetrafluoroiodobenzene (Figure 1e), the XB donor structure lacking para-substituted substitution. When matched with Bu_3PO, the 2,3,5,6-tetrafluoroiodobenzene XB donor exhibited ΔE_{int}, XBD, and Θ values most comparable to IPFB (Table 2), which suggests that it remains capable of promoting significant XB interactions. Geometry-optimized XB adducts for all XB donors with the common XB acceptor Bu_3PO are provided in the Supporting Information (Figures S17 and S18).

The effect of varying fluorine substitution on XB strength was also assessed experimentally in solution using NMR titrations to examine the XB adducts of the XB donors (Figure 1, *left*) and the XB acceptor Bu_3PO. As demonstrated in prior studies,[43,44] the strength of XB interactions can be characterized by its respective association constant (K_a) derived from the binding isotherms collected during ^1H and ^{19}F NMR titrations in which XB donors at a constant concentration are systematically mixed in solution with increasing concentrations of XB acceptor Bu_3PO. During each NMR titration experiment with sequential samples, the ^1H and ^{19}F NMR chemical shifts of the ortho protons and fluorine, respectively, are monitored and plotted as a function of Bu_3PO concentration to yield binding isotherms. Curve-fitting these binding isotherms allows for the determination of K_a values (Supporting Information, p. S5) with larger values of K_a being indicative of stronger XB interactions. A representative NMR titration analysis for the XB adduct of 2,4,5,6-tetrafluoroiodobenzene (Figure 1e) and Bu_3PO is shown in Figure 2. It should be noted that binding isotherms reaching plateau as the XB donor is saturated with the XB acceptor are indicative of strong and specific XB interactions, while non-plateauing binding isotherms represent systems in which XB interactions are weak, transient, and likely dwarfed by other non-XB interactions.[43] Using this approach, XB donors with varying fluorine substitutions (Figure 1, *left*) were NMR-titrated with Bu_3PO to yield K_a values (Table 2) that largely reinforced the computational findings regarding the differently fluorine-substituted XB donors. Additional examples of NMR titration analysis for all these XB donors with Bu_3PO are provided in the Supporting Information (Figures S24–S26).

The experimental K_a results suggest that XB donors with at least three fluorine EWGs on the aromatic ring possess significant σ-holes for strong XB interactions. Notably, the binding isotherm for the system with only a difluorinated XB donor (2,6-difluoroiodobenzene, Figure 1b) did not plateau with increasing Bu_3PO concentration—indicative of weak, transient XB interactions. Most importantly for the present study, the NMR data reinforces the theoretical results: substantial XB donor ability is maintained in 2,3,5,6-tetrafluoroiodobenzene, a critical result given that both the ortho and para positions are often expected to significantly influence how much electron density is distributed at the 1 position (a property highly relevant to the σ-hole formation and XB strength).

These results can be compared with experimental and computational measurements by Sarwar et al. in which a limited number of 2,3,5,6-tetrafluoroiodophenyl XB donors para-substituted with varying electron-donating (e.g., methoxy and piperidine) or electron-withdrawing (e.g., phenyl and alkyne-phenyl) abilities were tested for XB interaction strength with a common acceptor and showed that substitution away from the para fluorine resulted in lower K_a values.[44] While Sarwar and co-workers did not attempt to delineate the importance of ortho and meta EWG substitutions, as was addressed in

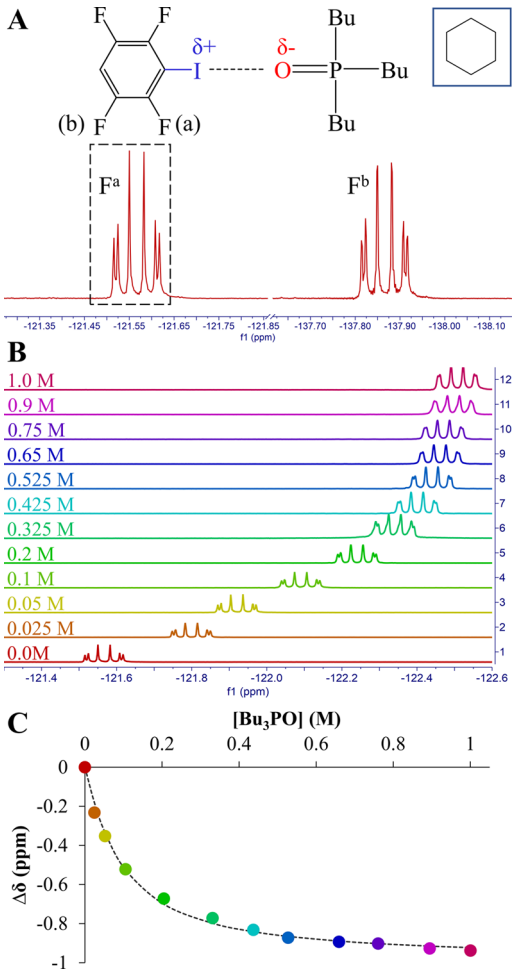

Figure 2. Representative NMR titration experiment for XB donor **2,3,5,6-tetrafluoroiodobenzene (2,3,5,6-TFIB)** (0.05 M) titrated with XB acceptor **tributylphosphine oxide (Bu_3PO)**, including (A) initial ^{19}F NMR spectrum of **2,3,5,6-TFIB** prior to titration, (B) change in the ortho F resonance shifts during the addition of increasing concentrations of **Bu_3PO**, and (C) corresponding binding isotherm used for non-linear regression analysis and determination of the association constant (K_a) that reflects the XB interaction strength of the adduct (solvent: **cyclohexane**).

https://doi.org/10.1021/acs.langmuir.2c00381
Langmuir XXXX, XXX, XXX−XXX

this study, their work did establish that the size of the σ-hole and ability of the XB-donor moiety $-C_6F_4I$ to engage in XB interactions were dependent on the electronic nature of the EWG at the para position. Our results thus far establish that the $-C_6F_4I$ moiety maintains a substantial σ-hole without the *para* fluorine EWG. However, it was uncertain if substitution at the *para* position for creating a ligand able to harness the $-C_6F_4I$ would negatively impact the XB-donor strength. With a plan of conducting amide coupling at the *para* position of $-C_6F_4I$, DFT calculations were conducted on two additional XB donors—one with an amide *para to* the XB-donor moiety and the other with an amide derivative of a thiol for potential attachment to Au-NPs. Specifically, DFT was used to study the interaction of 2,3,5,6-tetrafluoro-4-iodobenzamide and 2,3,5,6-tetrafluoro-4-iodo-*N*-(4-mercaptophenyl)benzamide with XB acceptor Bu_3PO. The results, shown in Table 2 (Figure S20, Supporting Information), indicate that in both cases, the para substitutions result in stronger XB-donor capability. With these results in mind, an amide-coupled, biphenyl thiolate ligand featuring the $-C_6F_4I$ moiety to engage in XB was designed for attachment to Au-NPs.

3.3. Strategic Design of the Thiol Ligands with $-C_6F_4I$ Moieties. The experimental results in this study and our prior work,[42,43] as well as other literature reports,[44] all suggest that the $-C_6F_4I$ moiety is able to act as an effective XB donor and promote strong XB interactions. The next step was to harness that interaction to Au-NPs, thereby establishing a link between XB and the unique optical and/or electronic properties of Au-NPs. A well-established approach for the specific modification of metallic Au-NPs is through the use of ω-functionalized thiol ligands that form Au−S bonds with the gold atoms comprising the NP core. While others have accomplished $-C_6F_4I$ functionalization of aqueous Au-NPs via electrostatic linkages, we know of no other reports in the literature of a thiolate ligand offering the terminal $-C_6F_4I$ group. As such, a primary goal of this project was the non-trivial synthesis of a stable thiolate ligand featuring the $-C_6F_4I$ functionality and sufficient length to effectively modify non-aqueous MPCs.

Our synthetic scheme for the desired thiolate ligand is presented in Scheme 1 with detailed procedures and structural information provided in Section 2.6 of Experimental Section and the Supporting Information (Figures S1−S10), including extensive ^1H and ^{19}F NMR, IR, UV−vis, and HRMS characterization of intermediates and the final product (Scheme 1—[**5**]). The final biphenyl amide-linked thiolate ligand (Scheme 1—[**5**]) was obtained in high yields and was strategically designed with several advantageous structural elements for the intended use of functionalizing MPCs with XB-donor functionality. First, the thiol terminus enables the ligand to attach to the MPCs via strong S−Au bonds formed during MPC ligand place-exchange procedures.[68,74] Second, the $-C_6F_4I$ moiety in the ligand is opposed on the ring by an amide linkage in the para position with the carbonyl part of the amide directly connected to the ring (Scheme 1—[**5**]). The carbonyl is expected to behave as a strong EWG, thereby contributing to and maintaining a larger, more partially positively charged σ-hole at the iodine atom to promote strong XB interactions. Reinforcing this hypothesis, DFT calculations of both 2,3,5,6-tetrafluoro-4-iodobenzamide (possessing the $-C_6F_4I$ moiety and the *para*-substituted amide group) and the complete thiolate ligand [**5**] as XB donors show strong interactions with the XB acceptor, Bu_3PO (Table 2 and Supporting Information, Figure S20). The presence of the amide bond, which has a partial double-bond characteristic, connecting two phenyl rings also confers both rigidity and length to the ligand, allowing the $-C_6F_4I$ moiety to protrude into solution beyond the peripheral, protective hexanethiol ligands of the as-prepared MPCs (C6-MPCs). With this design, the σ-hole of the XB-donor moiety $-C_6F_4I$ is prominently presented out in solution to engage in consistent, strong XB interactions with targeted analyte molecules in solution.

In addition to traditional synthetic confirmation of the ligand (e.g., NMR and IR spectra in the Supporting Information as well as HRMS), it was critical to observe if the synthesized ligand exhibited thiolate ligand behavior at gold interfaces. To establish thiolate behavior, traditional electrochemical characterization of gold substrates after exposure to our synthesized thiolate ligand (Scheme 1—[5]) was performed.[6,71] More specifically, non-Faradaic charging current measurements in buffer and cyclic voltammetry (CV) of $K_3Fe(CN)_6$ in solution were monitored and compared at gold electrodes before and after exposure to the synthesized ligand to establish if ligand exposure resulted in the formation of a self-assembled monolayer (SAM). Non-Faradaic charging current arising from the electric double layer at the interface of the electrode is particularly sensitive to the thickness and dielectric of the electrode's double layer, both of which are drastically altered when a SAM forms at the interface that introduces low dielectric medium separation between the two planes of charge.[75,76] Similarly, diffusional CV of a solution molecule such as $K_3Fe(CN)_6$ will exhibit unimpeded redox activity at a bare gold interface (i.e., reversible voltammetry) but show large increases in peak separation (ΔE_p) and lower current, consistent with the slower electron-transfer (ET) kinetics of a molecule at a SAM-modified electrode.[75] Figure 3 shows the electrochemical results

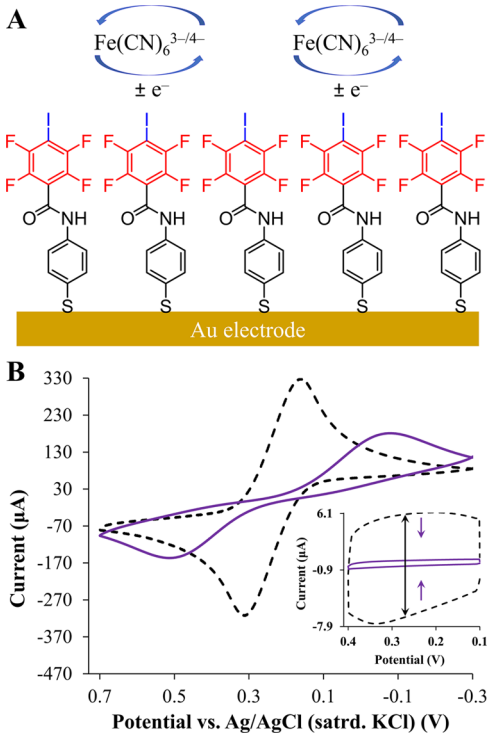

Figure 3. (A) Schematic of the self-assembled monolayer-modified gold electrode formed from 2,3,5,6-tetrafluoro-4-iodo-*N*-(4-mercaptophenyl)benzamide ligand [**5**] synthesized in Scheme 1 and probed with potassium ferricyanide probe electrochemistry and (B) cyclic voltammetry of bare and SAM−[**5**]-modified electrode in 5 mM potassium ferricyanide solution (0.5 M KCl) and supporting electrolyte (0.25 M PBS, inset).

for these experiments with the synthesized ligand [**5**] and indicates that the ligand does interact with the gold substrate and have thiol/thiolate behavior (i.e., oxidizing to form SAM-modified gold). Specifically, upon exposing bare gold to a solution of the ligand [**5**], there is a significant decrease in interfacial charging current (Figure 3B, *inset*) coupled with more irreversible CV for the $Fe(CN)_6^{3-/4-}$ redox couple. In combination with the structural characterization of the ligand, the electrochemical results represent strong evidence for the successful synthesis of the desired thiolate ligand with the $-C_6F_4I$ functionality.

3.4. XB Functionalization of MPCs via Ligand Place-Exchange Reactions. C6-MPCs were synthesized via the well-established Brust-style synthetic procedures (Section 2.7 of Experimental Section) and characterized as in prior work[6] and literature.[20,21,70] MPCs are a class of Au-NPs particularly well known

https://doi.org/10.1021/acs.langmuir.2c00381
Langmuir XXXX, XXX, XXX−XXX

for their stability, ease of use in organic solvents, and characteristic broad SPB resonance at ~518 nm in their UV−vis spectrum, an absorption band with known sensitivity to the NPs' surrounding chemical environment (Figure 4A).[20,21,70] Additionally, MPCs are

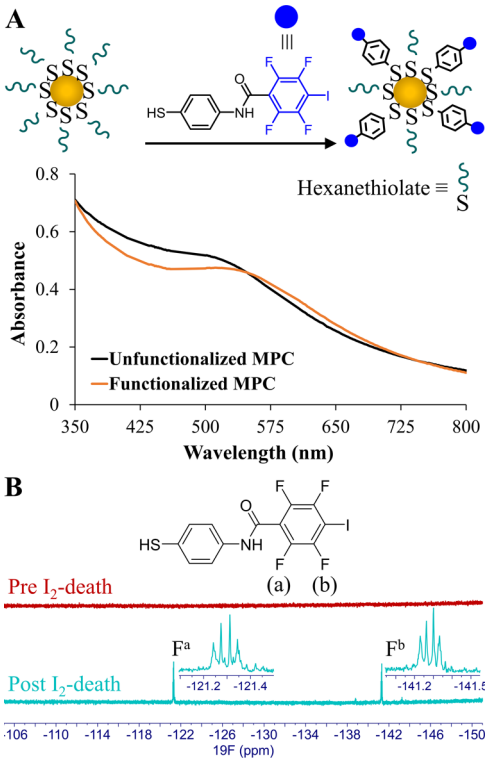

Figure 4. (A) UV−vis spectra of the as-prepared (unfunctionalized) hexanethiolate-protected gold nanoparticles (MPCs) before and after place-exchange reaction (inset schematic) with ligands [**5**] showing the resulting shift in SPB and (B) ^{19}F NMR spectra of the SEC-purified MPC-exchange reaction mixture in DMSO-d_6 before and after treatment with I_2 to liberate peripheral ligands as disulfides.

well known for being easily functionalized via well-established ligand-exchange reactions with thiolate ligands in solution.[68,74] As described in the Experimental Section, place-exchange reactions of as-prepared C6-MPCs mixed with the synthesized XB-donor ligand (Scheme 1—[**5**]) featuring the $-C_6F_4I$ moiety were conducted for this study. Aliquots of the place-exchange mixture were collected and rotary-evaporated at set time intervals to create samples with varying degrees of ligand functionalization. Aliquots were re-solvated before purification (removal of free ligands from f-MPCs) through published SEC techniques specific to MPCs (Supporting Information, pp. S19−S22).[69] Upon functionalization with the thiolate ligand [**5**], the f-MPC's SPB peak exhibited a notable red shift (Figure 4A) consistent with significant changes to the MPC surface dielectric that have often been observed in other literature reporting place-exchange functionalization of MPCs.[77] NMR spectroscopy was used to verify MPC functionalization as well as the relative degree of average functionalization. The resonance peaks of ^{1}H NMR spectra of peripheral ligands of the as-prepared C6-MPCs and f-MPCs in solution are typically dampened and exhibit severe broadening due to the proximity of the peripheral ligand structure to the surface of Au-NPs, whose electronic environment can be altered by the magnetic field (Supporting Information, Figures S11-A and S16-A). It is only after the samples are treated with iodine, which liberates the MPC's peripheral ligands as disulfides (i.e., I_2 "death" reactions), that resonance signals become sharpened and reflect structural details of ligands (see the Supporting Information, Figure S16B). In this case, the fluorines of the $-C_6F_4I$ moiety and the aromatic protons of the thiolate ligand [**5**] allow for the use of ^{19}F and ^{1}H NMR spectroscopy, respectively, to verify and quantify the extent of MPC functionalization. Post-place exchange, f-MPC samples showed no characteristic NMR peaks attributable to the XB-donor ligand [**5**] such as the ^{1}H NMR aromatic or amide protons or the ^{19}F NMR resonance from the $-C_6F_4I$ moiety (Figure 4B, *top*). However, as shown in Figure 4B (*bottom*), upon the I_2 treatment of the same samples, ^{19}F NMR spectroscopy revealed two signals attributable to the ortho and meta fluorines of the $-C_6F_4I$ moiety—a strong indicator that ligands were successfully exchanged onto the MPCs to create f-MPCs. Additionally, ^{1}H NMR shifts for the aromatic and amide protons were also observed after I_2 treatment with spectral examples provided in the Supporting Information (Figure S16B). The *relative* degree of MPC functionalization with the thiolate ligand [**5**] for each aliquot was determined by integrating ^{1}H NMR signals, determining the ratio of aromatic protons ($\int$ = 2 Hs) from the XB-donor ligand to the $-CH_3$ terminal group ($\int$ = 3 Hs) from the hexanethiol (protective ligand), and applying the ratio to the total ligands expected for the average MPC composition.[67] Additional details of such analysis process and the corresponding calculations for the degree of ligand functionalization can be found in the Supporting Information (Figure S16). It was determined that exposing the as-prepared MPCs to the XB-donor ligand [**5**] molecules for 5 days consistently resulted in an average of 50% ligand-exchange functionalization and the remainder of the study was conducted using that f-MPC material (see the Experimental Section for more details).

3.5. Assembled Films of Functionalized MPCs for XB Interactions. It was critical to evaluate if modifying the as-prepared MPCs with the synthesized XB-donor ligand [**5**] to make f-MPCs transferred the XB-donor capability onto f-MPCs to engage in XB interactions. There have been significant investigations of MPC film assemblies at electrodes,[23,40,41,78] including reports from our own laboratory using the films as platforms to study interparticle ET,[24] protein adsorption,[6,71] and sensing platforms.[79] In most cases, a multilayer MPC film is constructed at a SAM-modified gold electrode through layer-by-layer (LbL) assembly procedures involving alternating exposures to XB-donor f-MPCs, followed by a solution of linking ligands—each set of exposures referred to as a "dip cycle". For this study, it was hypothesized that the film assemblies of the f-MPCs could be used to probe for specific interfacial interactions such as XB. To test this hypothesis, hexanethiol SAM-modified gold electrodes were alternatingly exposed to a solution of nonanedithiol (NDT) (a linking ligand), followed by immersion in a solution of the f-MPCs or unfunctionalized MPCs (unf-MPCs), with the latter serving as a control film. NDT exposure displaces some hexanethiols from the SAM to form a mixed SAM with terminal thiols from NDT protruding from the modified electrode. Upon exposure to a f-MPC solution, the mixed SAM can immobilize f-MPCs at the interface to form a NP layer. "Dip cycle" sequences were performed twice to ensure coverage of the film surface with a f-MPC layer (Scheme 2A); a detailed description of the procedure is provided in the Experimental Section. As demonstrated in prior reports,[6,71] the LbL assembly of MPCs at an electrode can be verified and monitored with two well-established methods already used in the current study: (1) monitoring non-Faradaic charging current in the supporting electrolyte after each dip cycle and (2) observing the CV of a solution redox probe such as $K_3Fe(CN)_6$. With SAM formation at a gold substrate, charging current significantly decreases compared to that of a bare electrode (Figure 3B) and then, as has been previously observed,[6,71] systematically increases as MPCs, acting as small capacitors, are attached and assembled at the SAM-modified electrode. Similarly, CV of freely diffusing $Fe(CN)_6^{4-}$ at a SAM-modified electrode versus a bare electrode should exhibit dramatic blocking behavior with increased ΔE_p and diminished peak current as was observed in Figure 3B. Additional attachment of f-MPC layers to the SAM-modified electrode, however, will further enhance that effect as $Fe(CN)_6^{4-}$ access to the electrode becomes even more restricted. With successful formation of f-MPC film assemblies at electrodes, they can be employed for the electrochemical detection of XB interactions with target molecules in solution.

https://doi.org/10.1021/acs.langmuir.2c00381
Langmuir XXXX, XXX, XXX−XXX

Scheme 2. Functionalized MPC Dithiol-Linked Film Assembly Formed at a C6/NDT SAM-Modified Electrode (A) before and (B) after Exposure to XB-Acceptor Molecules (*Red*)

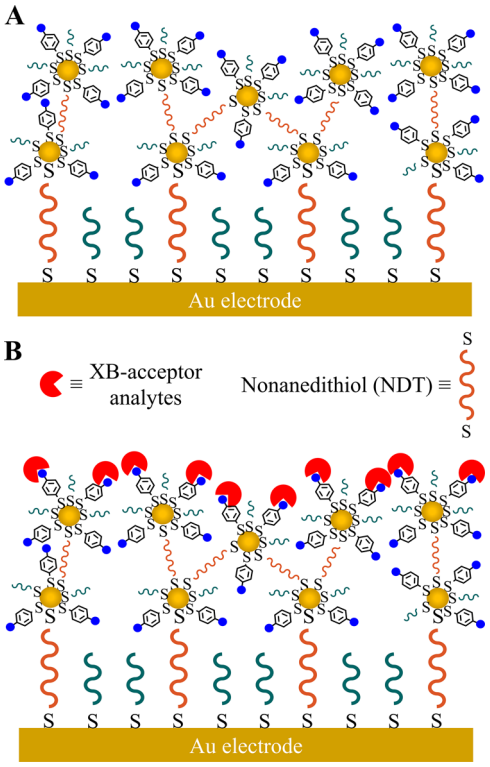

For these experiments, film assemblies of both XB-donor f-MPCs and unf-MPCs (control) were formed at electrodes with their assembly verified electrochemically as described. The MPC-film-modified electrodes (Scheme 2A) were then exposed to solutions of different analytes, including strong XB acceptors such as DABCO and trioctylphosphine oxide (Oct_3PO), a weak XB acceptor (Bu_2CO), and a non-XB-acceptor molecule (cyclohexane),[43] before being rinsed and remeasured electrochemically for charging current and $Fe(CN)_6^{3-/4-}$ blocking behavior. XB-donor f-MPC film assemblies should bind the strong XB acceptors (DABCO and Oct_3PO) as depicted in Scheme 2B and exhibit both the increased blocking behavior of $Fe(CN)_6^{3-/4-}$ and a simultaneous decrease in charging current compared to the system prior to exposure to the XB-acceptor molecules. In the absence of XB interactions between the film assemblies and analytes (e.g., Bu_2CO and cyclohexane), there should be little or no change in either of the electrochemical parameters after analyte exposure.

Figure 5 shows examples of typical electrochemical results for this type of experiment in which bare gold was modified with a hexanethiol (C6) SAM and subsequently further modified with a film of MPCs. In all cases, charging current behaves as expected, decreasing drastically from bare gold (not shown for figure clarity) to SAM modification before exhibiting small but systematic increases as MPC films are attached (Figure 5, *insets*). Simultaneously, CV of $Fe(CN)_6^{3-/4-}$ changed drastically from bare or clean gold to SAM-modified gold (indicative of the increasing blocking behavior), which subsequently became even more irreversible with the addition of the MPC layers (Figure 5A–D). The exposure of these films to different molecules in solution elicited different effects. For example, upon exposure to Oct_3PO, a strong XB-acceptor molecule, and subsequent rinsing before remeasurement, the charging current decreased significantly while the film simultaneously became more blocking toward $Fe(CN)_6^{3-/4-}$ (Figure 5A). Both results suggest that Oct_3PO formed a layer at the film interface through XB interactions. A similar trend can be routinely observed with the exposure of a similar film to DABCO, another strong XB acceptor molecule (Supporting Information, Figure S27), and the effect was highly repeatable in both cases.

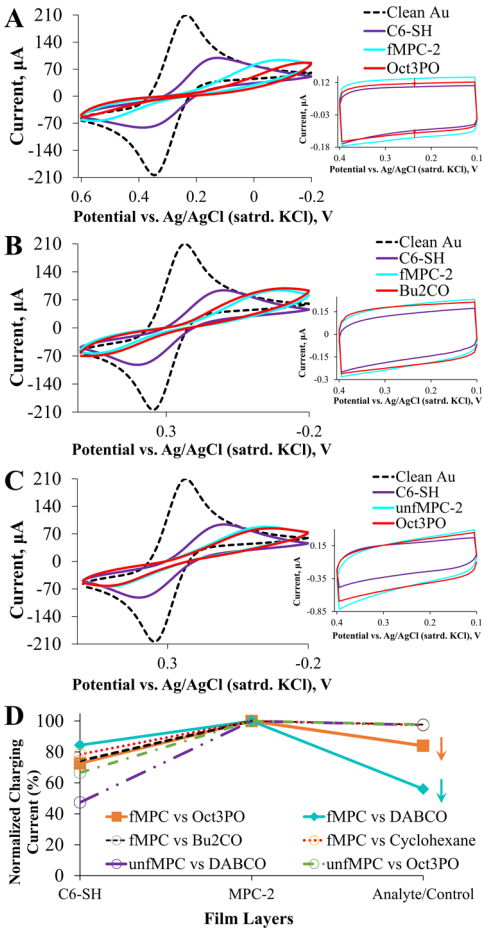

Figure 5. Cyclic voltammetry of 5 mM $K_3Fe(CN)_6$ in 0.5 M KCl (50 mV/s) and non-Faradaic charging current scans in 0.25 M PBS (**insets**; 100 mV/s) for *clean Au*, after hexanethiol-SAM modification (*C6-SH*), after C6-SH SAMs were further modified with MPC film assemblies (e.g., *f-MPC-2*), and after exposure to (A) Oct_3PO, a strong XB acceptor, at f-MPC films; (B) Bu_2CO, a weak XB acceptor at f-MPC films; (C) Oct_3PO at unf-MPC films; and (D) summary of normalized charging current measurements showing decreases only when at f-MPC films were exposed to strong XB acceptor molecules (Oct_3PO and DABCO).

Control experiments were also conducted to reinforce that the results with Oct_3PO and DABCO were the result of XB interactions. Specific controls included analogous experiments exposing the same f-MPC film assemblies to weak and non-XB acceptor molecules as well as incorporating unf-MPCs into films that were then exposed to strong XB-acceptor molecules. If the prior results were due to XB interactions, then they should not be repeatable to the same extent in these control experiments. Figure 5B shows the results of the same experiment with exposure of f-MPC film assemblies to Bu_2CO, a weak XB-acceptor molecule. Notably, there was essentially no significant change in both the charging current or the $Fe(CN)_6^{3-/4-}$ blocking behavior, results suggesting that, unlike the strong XB acceptors, a layer of Bu_2CO molecules was *not* interacting with the f-MPC film interface. A similar trend is observed when cyclohexane, a non-XB molecule, was exposed to a film of f-MPCs in which no change in charging current or $Fe(CN)_6^{3-/4-}$ blocking was detected (Supporting Information, Figure S28). As a final control, the same experiment using a film comprised of unf-MPCs, which lack the functionality to engage in XB interactions, resulting in no significant change in charging current or blocking behavior upon exposure to both Oct_3PO (Figure 5C) or DABCO (Supporting Information, Figure S29).

https://doi.org/10.1021/acs.langmuir.2c00381
Langmuir XXXX, XXX, XXX−XXX

Figure 5D summarizes the consistently observed charging current trends from the electrochemical experiments and the control systems, which show increases in charging current from SAMs to films of f-MPCs, followed by decreases in charging current that occurred only when the f-MPC film assemblies engaged in strong XB interactions with XB-acceptor molecules in solution (i.e., Oct_3PO and DABCO).

3.6. XB-Induced Aggregation of Au-NPs—Molecular Detection Scheme. NP aggregation occurs when a chemical event causes significantly decreased interparticle spacing in solution, thereby bringing NPs in close enough proximity to transition their optical properties from that of individual NPs to that of NP aggregates. When this transition is instigated by the presence of a specific analyte that can interact with the peripheral ligands on more than one NP from multiple directions, the SPB is observed to red shift or diminish and is often coupled with visible changes in solution color and/or precipitation of aggregate materials that experience a sudden change in solubility as they coagulate. NP aggregation can also be readily visualized with TEM imaging that shows individual NP transition to large agglomerates. In this respect, analyte-induced NP aggregation represents a relatively simple and sensitive strategy for molecular detection schemes requiring (1) successful functionalization of NPs with a specific ligand that can promote an intermolecular interaction and (2) an analyte receptive to that specific interaction. As previously mentioned, aqueous NP-based aggregation schemes are quite common[1] but we are unaware of analogous reports using non-aqueous NPs such as alkanethiolate-MPCs and employing XB interactions to induce an aggregation event.

Building upon our electrochemical evidence that the XB-donor f-MPCs featuring ligands with $-C_6F_4I$ moiety can engage in XB interactions with XB-acceptor analytes, proof-of-concept experiments were designed for the detection of DABCO in solution via XB-induced MPC aggregation. As depicted in Scheme 3, DABCO, with

Scheme 3. Illustration of the f-MPC Aggregation Event in Solution due to the Presence of the XB Acceptor (DABCO)

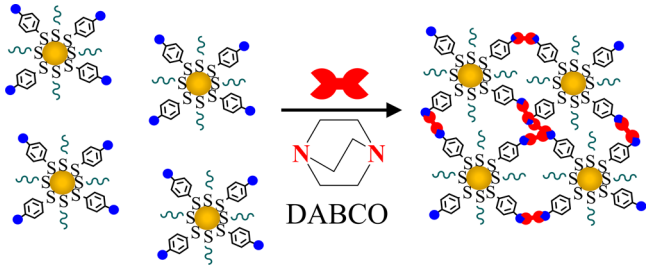

the two opposing tertiary amines (i.e., XB-acceptor binding sites), can bridge between multiple f-MPCs. The multiple XB-acceptor binding sites afford the system a rudimentary selectivity as well. In a typical experiment, dilute solutions of f-MPCs were exposed to incrementally increasing amounts of added DABCO (0–3.5 mM). Visualized with UV–vis spectroscopy, Figure 6A shows that the addition of DABCO to a f-MPC solution (A_{518} = 1.0 a.u.) caused a systematic red-shifted (originally at ~518 nm) and diminished SPB with a simultaneous increase in absorbance at higher wavelengths (~725 nm). Both of these observations are consistent with NP aggregation events.[1] Shifts in the SPB were rapid, occurring minutes after adding DABCO (1 mM). Adding higher DABCO concentrations to the solution amplified the observed effect. The typically dark f-MPC solutions were notably clear after DABCO was added and, if left to sit undisturbed overnight, the MPC-DABCO mixtures exhibited significant precipitation of MPC aggregates to the bottom of the sealed cuvette. This "crash-out" of the f-MPC material could be physically agitated and resuspended temporarily (~15 min). Control experiments conducted without the addition of DABCO and left to sit undisturbed over the same amount of time yielded no spectroscopic changes or visual precipitation of the f-MPC material. The examples of these visual observations are shown in Figure 6B. UV–vis spectra collected immediately after physical disruption of the precipitate

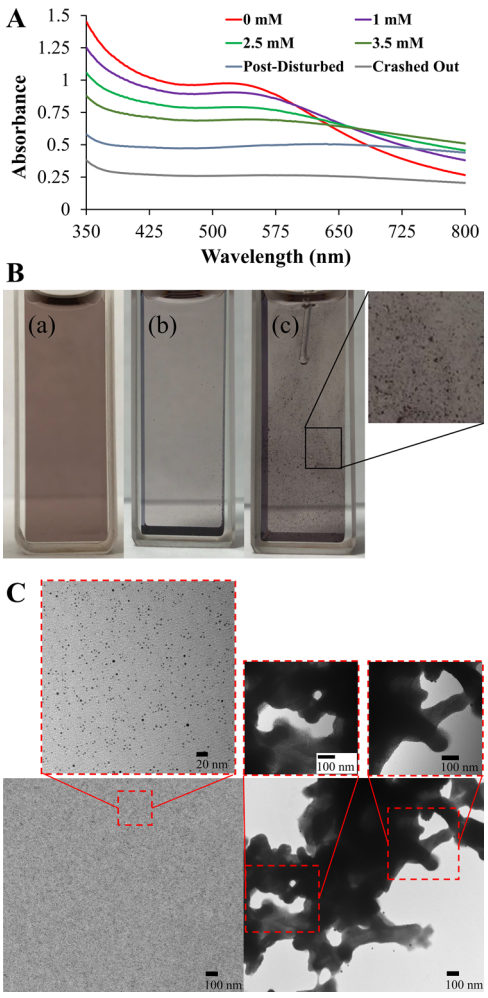

Figure 6. (A) UV–vis spectra of solutions of f-MPCs (capable of XB interactions) with varying concentrations of DABCO (XB acceptor with two binding sites) over time. (B) Pictures of f-MPC solution (a) before and (b) after the addition of DABCO, with the latter resulting in a layer of precipitated MPC aggregates at the bottom of the cuvette that can then be (c) resuspended with physical disruption with a pipette before resettling. (C) TEM images of f-MPCs before (*left*) and after (*right*) exposure to DABCO.

resulted in higher absorbances at longer wavelengths (Figure 6A), indicative of MPC aggregates being temporarily resuspended before resettling on the bottom of the cuvette. The XB-induced MPC aggregation by DABCO was also visualized with TEM imaging analysis, with images of the f-MPCs in the absence and presence of DABCO (Figure 6C) confirming the aggregation event. Specifically, prior to the addition of 1 mM DABCO, TEM imaging showed individualized f-MPCs with no interparticle interaction, while the addition of DABCO resulted in large aggregates in which individual f-MPCs were no longer visible.

With any NP aggregation molecular detection scheme, it is critical to conduct control experiments so that the mechanism of aggregation can be isolated to the specific targeted interaction, which in this case is XB. Two control experiments were conducted: (1) unf-MPCs with DABCO (featuring two XB-acceptor binding sites) and (2) f-MPCs with Oct_3PO (featuring only one XB-acceptor binding site). If XB interactions are driving the observed aggregation events with DABCO, the first control experiment should elicit no change in the unf-MPC solution since the MPCs are not capable of engaging as XB donors, while the second control experiment with Oct_3PO employs a strong XB acceptor with only one binding site that is incapable of bridging between f-MPCs and thus should also result in no NP

https://doi.org/10.1021/acs.langmuir.2c00381
Langmuir XXXX, XXX, XXX–XXX

aggregation, regardless of time or XB acceptor concentration. The results of both control experiments are displayed in Figure 7. The first

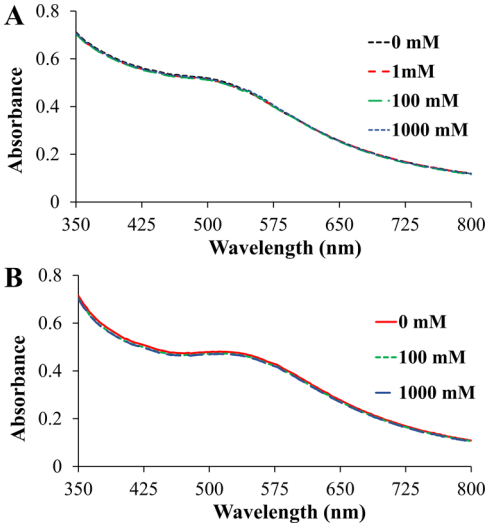

Figure 7. UV−vis spectra of solutions of (A) unfunctionalized or as-prepared MPCs (not capable of XB interactions) with varying concentrations of DABCO (XB acceptor with two binding sites) over at least 3 days and (B) f-MPCs (capable of XB interactions) with varying concentrations of Oct_3PO (XB acceptor with one binding site) over at least 3 days.

experiment with unf-MPC solution (A_{518} = 0.5 a.u), monitored for 3 days after the addition of DABCO, displayed no spectral changes even after increasing the DABCO concentration to 1 M. This result demonstrates that the unf-MPCs, without XB-donor capability, cannot engage in XB interactions with DABCO. The second control experiment with f-MPCs (A_{518} = 0.5 a.u.) and Oct_3PO also produced no changes in the UV−vis spectra after the addition of the Oct_3PO acceptor (whose concentration was also increased up to 1 M). With only one binding site, the Oct_3PO molecule is likely to bind to f-MPCs via XB interactions but ultimately is unable to bridge between f-MPCs and decrease interparticle spacing. An important implication of both control experiments is to establish that the aggregation phenomenon seen with f-MPCs and DABCO was not a result of solubility issues but, instead, was caused by specific XB interactions between DABCO and the f-MPCs.

Additional measurements of XB interactions between DABCO and f-MPCs were made with DOSY NMR to further establish the viability of applying such a method to interactions at the periphery of NPs in solution.[80] A set of 10 additional DOSY NMR measurements, including a number of control experiments, were conducted with f-MPCs (A_{518} = 0.5 a.u.) as well as unf-MPCs (A_{518} = 0.5 a.u.) acting as XB donors or non-XB donors, respectively, with 5 mM DABCO. The results of these experiments are summarized in Table 3 where it is again conducive to refer to the experiment number listed in the first column for the following discussion. For baseline measurements, the log D value of 5 mM DABCO in toluene-d_8 was measured to be −8.64, and the control log D value of the residual toluene-d_7h_1 was found to be −8.56 (experiments **#1** and **#2**, Table 3), both of which were expected given the difference in molecular sizes and consistent with prior measurements (Table 1). Notably in experiments **#3** and **#4** (Table 3), the measured log D values of DABCO are markedly different 15 min after being mixed with unf-MPCs (−8.55) versus f-MPCs (−8.66), a result attributable to DABCO interacting with the f-MPCs via XB interactions and significantly slowing down in solution. If the measurement of log D values of 5 mM DABCO is done in the presence of f-MPCs over time, one can hypothesize that there would be an initial decrease in DABCO mobility as the XB interactions form but, as the f-MPC material aggregates and precipitates, the DOSY measurement at a later time would return to reflecting the log D value

Table 3. DOSY NMR Measurements of Diffusion Coefficients (D) of DABCO (5 mM) in the Presence of unf-MPCs and f-MPCs (Solvent: Toluene-d_8)[a]

#	XB donor	target	log D (log(m^2/s))
1	none	^{1}H toluene-d_7h_1	−8.56 (±0.07)
2	none	^{1}H DABCO	−8.64 (±0.07)
3	unf-MPCs	^{1}H DABCO	−8.55 (±0.05)
4	f-MPCs (15 min)	^{1}H DABCO	−8.66 (±0.05)
5	f-MPCs (4 h)	^{1}H DABCO	−8.60 (±0.06)
6	f-MPCs (12 h)	^{1}H DABCO	−8.55 (±0.05)
7	unf-MPCs	^{1}H toluene-d_7h_1	−8.55 (±0.08)
8	f-MPCs (15 min)	^{1}H toluene-d_7h_1	−8.55 (±0.10)
9	f-MPCs (4 h)	^{1}H toluene-d_7h_1	−8.55 (±0.09)
10	f-MPCs (12 h)	^{1}H toluene-d_7h_1	−8.55 (±0.07)

[a]Concentrations of unf-MPCs and f-MPCs are equivalent to A_{518} = 0.50 a.u. DOSY NMR measurements of the sample of 5 mM DABCO and unf-MPCs were carried out at the same time intervals as the sample with f-MPCs; the log D values of DABCO and toluene-d_7h_1 in the unf-MPC sample were constant over time (12 h).

of freely diffusing DABCO that is *not* interacting with f-MPCs. With the sample of DABCO and f-MPCs, the log D values of DABCO represented in experiments **#4**, **#5**, and **#6** (Table 3) were measured at 15 min, 4 h, and 12 h, respectively, after the initial sample preparation. The results found in these experiments (**#4**, **#5**, and **#6**) support the previously stated hypothesis. At the 15 min mark, the log D value of DABCO was −8.66 (experiment **#4**, Table 3), suggesting that DABCO had slower mobility as it engaged in XB interactions with f-MPCs in solution. After 4 h, DABCO's log D value increased to −8.60 (experiment **#5**, Table 3), and there was a small amount of f-MPC aggregate in the NMR tube—results that indicate that DABCO induced partial f-MPC aggregation while the remaining DABCO amount in solution was still interacting with other f-MPCs in solution. The log D value of DABCO increased to −8.55 after 12 h (experiment **#6**, Table 3)—with visible, significant precipitation of the f-MPC material in the tube and the solution becoming clearer—which is more representative of freely diffusing DABCO not engaging in XB interactions. Control experiments monitoring the log D values of residual toluene-d_7h_1 in solutions of only 5 mM DABCO (experiment **#1**), 5 mM DABCO with unf-MPCs (experiment **#7**), and 5 mM DABCO with f-MPCs over time (experiments **#8**−**#10**) showed no appreciable difference in their log D values. This study has established DOSY NMR as a tool that can probe intermolecular interactions occurring at the periphery of non-aqueous NPs like MPCs.

While mM and μM concentrations of DABCO instigated significant MPC aggregation with obvious spectral shifts and eventual precipitation (Figure 6), evidence of molecular recognition at much lower DABCO concentrations was also achieved with detection of f-MPC agglomeration. As displayed in Figure 8, small spectral shifts of the SPB were observed, and f-MPC agglomeration was visualized with TEM imaging after the addition of only 100 nM DABCO. At this low concentration of DABCO, agglomeration of f-MPCs occurred, but the fledgling aggregates remained suspended in the solution (i.e., there was no observable mass aggregation of the f-MPC material as can be seen in Figure 6 with higher concentrations of DABCO). Even without aggregation, however, TEM imaging confirms the f-MPC agglomeration (Figure 8B). Moreover, even at 100 nM DABCO and in the presence of a lower f-MPC concentration, it was significantly more challenging to find individual f-MPCs during the sampling of the TEM grid field. Similar experimental results were found with 50 nM DABCO, but, as expected, it was relatively easier to visualize individual (i.e., non-agglomerated) f-MPCs in the TEM images (Supporting Information, Figure S31). Control experiments of f-MPCs in solution (A_{518} = 0.2 a.u.) with no added DABCO showed no UV−vis spectral change over 4 days of monitoring (Supporting

https://doi.org/10.1021/acs.langmuir.2c00381
Langmuir XXXX, XXX, XXX−XXX

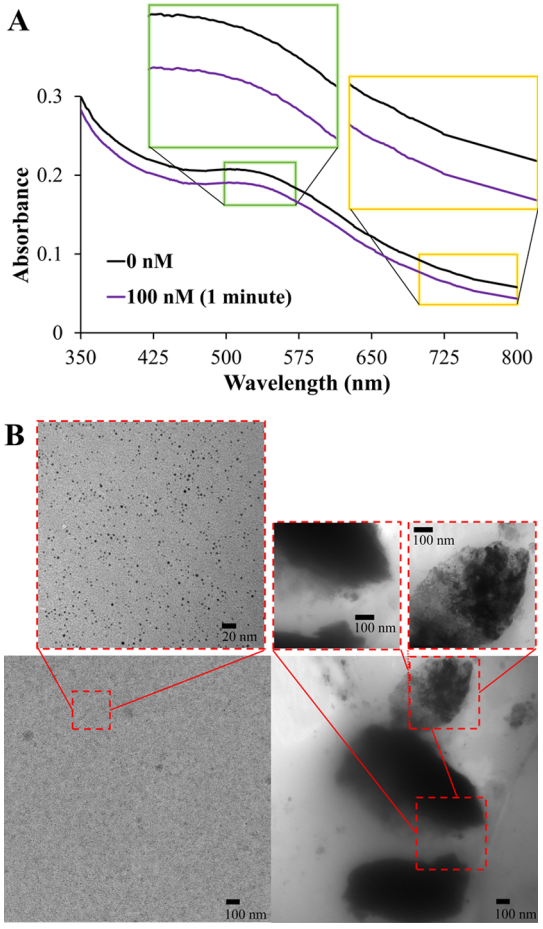

Figure 8. (A) UV−vis spectra and (B) TEM imaging before (*left*) and after (*right*) the addition of 100 nM DABCO to a solution of f-MPCs, resulting in a small diminishment of the SPB accompanied by the corresponding agglomerated NPs—both effects were absent in control measurements (Supporting Information, Figure S30). Note: The results were unchanged over 3 days.

Information, Figure S30). Based on the overall experimental results, it was reasonable to project a LOD for this method to be at ∼50−100 nM for strong XB-acceptor molecules.

4. CONCLUSIONS

The major conclusions of this study are manifold: establishing the experimental and theoretical exploration of an XB-capable molecular structure with various methods; successfully synthesizing a novel thiolate XB-donor ligand and attaching the ligand to the periphery of Au-MPCs; and demonstrating the electrochemical, NMR, microscopy, and optical measurements/evidence of XB interactions between f-MPCs and target molecules. The study connects a fundamental study of XB interactions to a proof-of-concept, non-aqueous NP system with a demonstrated ability to provide molecular recognition signaling at nanomolar concentrations. Higher analyte concentrations instigate NP aggregation to a level that would allow for the use of the strategy in portable testing kits used in the field to target a wider solubility range of analyte molecules capable of engaging in XB interactions, including previously inaccessible less-polar targets that have a molecular profile to engage in XB interactions (i.e., two more XB acceptor sites). This work represents a foundation to expand the methodology and use of NP detection systems to further exploit XB as a feasible mechanism for the detection of damaging pesticides or as a preliminary screening forensic test for certain narcotics—providing an additional tool for environmental, criminalistics, and medical fields.[29,45,50,81]

■ ASSOCIATED CONTENT

Supporting Information

The Supporting Information is available free of charge at https://pubs.acs.org/doi/10.1021/acs.langmuir.2c00381.

Details of DFT analysis, DOSY NMR measurements, NMR titrations, non-linear regression method for determining the K_a values, SEC procedures for MPC purification, and characterization of MPC functionalization; ^{19}F and ^{1}H NMR and IR spectra of synthesized intermediates and the final product; UV−vis spectra and TEM imaging analyses of f-MPCs and unf-MPCs in control and experimental systems; cyclic voltammetry and non-Faradaic charging current scans of f-MPC and unf-MPC films; optimized geometries of all XB adducts; initial ^{19}F and ^{1}H spectra of all XB donors; and binding isotherms (or titration curves) from NMR titration experiments (PDF)

■ AUTHOR INFORMATION

Corresponding Author

Michael C. Leopold − *Department of Chemistry, Gottwald Center for the Sciences, University of Richmond, Richmond, Virginia 23173, United States;* orcid.org/0000-0001-6525-9281; Phone: +1-(804)-287-6329; Email: mleopold@richmond.edu

Authors

Quang Minh Dang − *Department of Chemistry, Gottwald Center for the Sciences, University of Richmond, Richmond, Virginia 23173, United States*

Samuel T. Gilmore − *Department of Chemistry, Gottwald Center for the Sciences, University of Richmond, Richmond, Virginia 23173, United States*

Karthik Lalwani − *Department of Chemistry, Gottwald Center for the Sciences, University of Richmond, Richmond, Virginia 23173, United States*

Richard J. Conk − *Department of Chemistry, Gottwald Center for the Sciences, University of Richmond, Richmond, Virginia 23173, United States;* orcid.org/0000-0001-7803-4532

Jeffrey H. Simpson − *Department of Chemistry, Gottwald Center for the Sciences, University of Richmond, Richmond, Virginia 23173, United States*

Complete contact information is available at: https://pubs.acs.org/10.1021/acs.langmuir.2c00381

Funding

The research was generously supported by the National Science Foundation (CHE-2101010), the Arnold and Mabel Beckman Foundation (Q.M.D.), the Virginia Foundation for Independent Colleges Mednick Memorial Fellowship (M.C.L., S.T.G., and K.L.), the Camille & Henry Dreyfus Foundation (M.C.L.), and the Floyd D. and Elisabeth S. Gottwald Endowment (M.C.L.) and funding from the College of Arts and Sciences at the University of Richmond.

Notes

The authors declare no competing financial interest.

https://doi.org/10.1021/acs.langmuir.2c00381
Langmuir XXXX, XXX, XXX−XXX

■ ACKNOWLEDGMENTS

The authors would like to acknowledge the assistance with this project from the following members of the University of Richmond (UR), Department of chemistry: Drs. Carol Parish (DFT calculations), Miles Johnson (synthesis consultation), and Michael Norris (synthesis consultation and Schlenk line usage) and undergraduate researchers Arjun Jaini, Tess Munoz, and Jared Thomas (ligand synthesis—bromide analogues). The authors are grateful to Drs. T. Leopold, W O'Neal, R. Coppage, Phil Joseph, Russ Collins, and LaMont Cheatham—all of whom make the research possible at the University of Richmond. This work was dedicated to the PI's incredible mentors over their career: Professors John Gupton (UR), William Myers (UR), Royce Murray (UNC-CH), Ed Bowden (NC State), and Roddy Amenta (James Madison University).

■ REFERENCES

(1) Vilela, D.; González, M. C.; Escarpa, A. Sensing colorimetric approaches based on gold and silver nanoparticles aggregation: Chemical creativity behind the assay. A review. *Anal. Chim. Acta* **2012**, *751*, 24−43.

(2) Pratap, D.; Soni, S. Review on the Optical Properties of Nanoparticle Aggregates Towards the Therapeutic Applications. *Plasmonics* **2021**, *16*, 1495−1513.

(3) Unser, S.; Bruzas, I.; He, J.; Sagle, L. Localized Surface Plasmon Resonance Biosensing: Current Challenges and Approaches. *Sensors* **2015**, *15*, 15684−15716.

(4) Priyadarshini, E.; Pradhan, N. Gold nanoparticles as efficient sensors in colorimetric detection of toxic metal ions: A review. *Sens. Actuators, B* **2017**, *238*, 888−902.

(5) Zamborini, F. P.; Bao, L.; Dasari, R. Nanoparticles in Measurement Science. *Anal. Chem.* **2012**, *84*, 541−576.

(6) Loftus, A. F.; Reighard, K. P.; Kapourales, S. A.; Leopold, M. C. Monolayer-protected nanoparticle film assemblies as platforms for controlling interfacial and adsorption properties in protein monolayer electrochemistry. *J. Am. Chem. Soc.* **2008**, *130*, 1649−1661.

(7) Sun, Y.; Mayers, B. T.; Xia, Y. Template-Engaged Replacement Reaction: A One-Step Approach to the Large-Scale Synthesis of Metal Nanostructures with Hollow Interiors. *Nano Lett.* **2002**, *2*, 481−485.

(8) Parashar, U. K.; Nirala, N. R.; Upadhyay, C.; Saxena, P. S.; Srivastava, A. Urease Immobilized Fluorescent Gold Nanoparticles for Urea Sensing. *Appl. Biochem. Biotechnol.* **2015**, *176*, 480−492.

(9) Isaacs, S. R.; Cutler, E. C.; Park, J.-S.; Lee, T. R.; Shon, Y.-S. Synthesis of tetraoctylammonium-protected gold nanoparticles with improved stability. *Langmuir* **2005**, *21*, 5689−5692.

(10) Painuli, R.; Raghav, S.; Kumar, D. Selective Interactions of Al(III) with Plasmonic AgNPs by Colorimetric, Kinetic, and Thermodynamic Studies. *ACS Omega* **2019**, *4*, 3635−3645.

(11) Zhou, X. T.; Wang, L. M.; Shen, G. Q.; Zhang, D. W.; Xie, J. L.; Mamut, A.; Huang, W. W.; Zhou, S. S. Colorimetric determination of ofloxacin using unmodified aptamers and the aggregation of gold nanoparticles. *Microchim. Acta* **2018**, *185*, 355.

(12) Du, G.; Wang, L.; Zhang, D.; Ni, X.; Zhou, X.; Xu, H.; Xu, L.; Wu, S.; Zhang, T.; Wang, W. Colorimetric aptasensor for progesterone detection based on surfactant-induced aggregation of gold nanoparticles. *Anal. Biochem.* **2016**, *514*, 2−7.

(13) Liu, Q.; Han, P.; Gong, W. W.; Wang, H.; Feng, X. Y. Colorimetric determination of the pesticide chlorothalonil based on the aggregation of gold nanoparticles. *Microchim. Acta* **2018**, *185*, 354.

(14) Jayeoye, T. J.; Cheewasedtham, W.; Putson, C.; Rujiralai, T. Colorimetric determination of sialic acid based on boronic acid-mediated aggregation of gold nanoparticles. *Microchim. Acta* **2018**, *185*, 409.

(15) Huang, P.; Li, J.; Liu, X.; Wu, F. Colorimetric determination of aluminum(III) based on the aggregation of Schiff base-functionalized gold nanoparticles. *Microchim. Acta* **2016**, *183*, 863−869.

(16) Templeton, A. C.; Chen, S.; Gross, S. M.; Murray, R. W. Water-Soluble, Isolable Gold Clusters Protected by Tiopronin and Coenzyme A Monolayers. *Langmuir* **1999**, *15*, 66−76.

(17) Doan, T. T.; Day, R. W.; Leopold, M. C. Optical and electrochemical properties of multilayer polyelectrolyte thin films incorporating spherical, gold colloid nanomaterials. *J. Mater. Sci.* **2012**, *47*, 108−120.

(18) Schmidt, A. R.; Nguyen, N. D. T.; Leopold, M. C. Nanoparticle Film Assemblies as Platforms for Electrochemical Biosensing-Factors Affecting the Amperometric Signal Enhancement of Hydrogen Peroxide. *Langmuir* **2013**, *29*, 4574−4583.

(19) Sokolowska, K.; Hulkko, E.; Lehtovaara, L.; Lahtinen, T. Dithiol-Induced Oligomerization of Thiol-Protected Gold Nanoclusters. *J. Phys. Chem. C* **2018**, *122*, 12524−12533.

(20) Sardar, R.; Funston, A. M.; Mulvaney, P.; Murray, R. W. Gold Nanoparticles: Past, Present, and Future. *Langmuir* **2009**, *25*, 13840−13851.

(21) Murray, R. W. Nanoelectrochemistry: Metal nanoparticles, nanoelectrodes, and nanopores. *Chem. Rev.* **2008**, *108*, 2688−2720.

(22) Templeton, A. C.; Wuelfing, W. P.; Murray, R. W. Monolayer-Protected Cluster Molecules. *Section Title: Surface Chemistry and Colloids* **2000**, *33*, 27−36.

(23) Zamborini, F. P.; Leopold, M. C.; Hicks, J. F.; Kulesza, P. J.; Malik, M. A.; Murray, R. W. Electron hopping conductivity and vapor sensing properties of flexible network polymer films of metal nanoparticles. *J. Am. Chem. Soc.* **2002**, *124*, 8958−8964.

(24) Tognarelli, D. J.; Miller, R. B.; Pompano, R. R.; Loftus, A. F.; Sheibley, D. J.; Leopold, M. C. Covalently networked monolayer-protected nanoparticle films. *Langmuir* **2005**, *21*, 11119−11127.

(25) Lin, D.; Liu, H.; Qian, K.; Zhou, X.; Yang, L.; Liu, J. Ultrasensitive optical detection of trinitrotoluene by ethylenediamine-capped gold nanoparticles. *Anal. Chim. Acta* **2012**, *744*, 92−98.

(26) Wang, F.; Lu, Y.; Chen, Y.; Sun, J.; Liu, Y. Colorimetric Nanosensor Based on the Aggregation of AuNP Triggered by Carbon Quantum Dots for Detection of Ag+ Ions. *ACS Sustain. Chem. Eng.* **2018**, *6*, 3706−3713.

(27) Lin, S.-Y.; Tsai, Y.-T.; Chen, C.-C.; Lin, C.-M.; Chen, C.-h. Two-Step Functionalization of Neutral and Positively Charged Thiols onto Citrate-Stabilized Au Nanoparticles. *J. Phys. Chem. B* **2004**, *108*, 2134−2139.

(28) Lin, S.-Y.; Liu, S.-W.; Lin, C.-M.; Chen, C.-h. Recognition of Potassium in Water by 15-Crown-5 Functionalized Gold Nanoparticles. *Anal. Chem.* **2002**, *74*, 330.

(29) Kumar, V.; Kumar, P.; Pournara, A.; Vellingiri, K.; Kim, K.-H. Nanomaterials for the sensing of narcotics: Challenges and opportunities. *TrAC, Trends Anal. Chem.* **2018**, *106*, 84−115.

(30) Jiang, Y.; Zhao, H.; Zhu, N.; Lin, Y.; Yu, P.; Mao, L. A Simple Assay for Direct Colorimetric Visualization of Trinitrotoluene at Picomolar Levels Using Gold Nanoparticles. *Angew. Chem. Int. Ed.* **2008**, *47*, 8601−8604.

(31) Dasary, S. S. R.; Senapati, D.; Singh, A. K.; Anjaneyulu, Y.; Yu, H.; Ray, P. C. Highly Sensitive and Selective Dynamic Light-Scattering Assay for TNT Detection Using p-ATP Attached Gold Nanoparticle. *ACS Appl. Mater. Interfaces* **2010**, *2*, 3455−3460.

(32) Wang, G.; Akiyama, Y.; Shiraishi, S.; Kanayama, N.; Takarada, T.; Maeda, M. Cross-Linking versus Non-Cross-Linking Aggregation of Gold Nanoparticles Induced by DNA Hybridization: A Comparison of the Rapidity of Solution Color Change. *Bioconjugate Chem.* **2017**, *28*, 270−277.

(33) Ai, K.; Liu, Y.; Lu, L. Hydrogen-Bonding Recognition-Induced Color Change of Gold Nanoparticles for Visual Detection of Melamine in Raw Milk and Infant Formula. *J. Am. Chem. Soc.* **2009**, *131*, 9496−9497.

(34) Darbha, G. K.; Singh, A. K.; Rai, U. S.; Yu, E.; Yu, H.; Chandra Ray, P. Selective detection of mercury (II) ion using nonlinear optical properties of gold nanoparticles. *J. Am. Chem. Soc.* **2008**, *130*, 8038−8043.

https://doi.org/10.1021/acs.langmuir.2c00381
Langmuir XXXX, XXX, XXX−XXX

(35) Cavallo, G.; Metrangolo, P.; Milani, R.; Pilati, T.; Priimagi, A.; Resnati, G.; Terraneo, G. The Halogen Bond. *Chem. Rev.* **2016**, *116*, 2478−2601.
(36) Politzer, P.; Murray, J. S.; Clark, T. Halogen bonding: an electrostatically-driven highly directional noncovalent interaction. *Phys. Chem. Chem. Phys.* **2010**, *12*, 7748−7757.
(37) Clark, T.; Hennemann, M.; Murray, J. S.; Politzer, P. Halogen bonding: the sigma-hole. *J. Mol. Model.* **2007**, *13*, 291−296.
(38) Tawfik, M.; Donald, K. J. Halogen Bonding: Unifying Perspectives on Organic and Inorganic Cases. *J. Phys. Chem. A* **2014**, *118*, 10090−10100.
(39) Parker, A. J.; Stewart, J.; Donald, K. J.; Parish, C. A. Halogen Bonding in DNA Base Pairs. *J. Am. Chem. Soc.* **2012**, *134*, 5165−5172.
(40) Shirman, T.; Kaminker, R.; Freeman, D.; van der Boom, M. E. Halogen-Bonding Mediated Stepwise Assembly of Gold Nanoparticles onto Planar Surfaces. *ACS Nano* **2011**, *5*, 6553−6563.
(41) Shirman, T.; Arad, T.; van der Boom, M. E. Halogen Bonding: A Supramolecular Entry for Assembling Nanoparticles. *Angew. Chem. Int. Ed.* **2010**, *49*, 926−929.
(42) Jaini, A. K. A.; Hughes, L. B.; Kitimet, M. M.; Ulep, K. J.; Leopold, M. C.; Parish, C. A. Halogen Bonding Interactions for Aromatic and Nonaromatic Explosive Detection. *ACS Sens.* **2019**, *4*, 389−397.
(43) Dang, Q. M.; Simpson, J. H.; Parish, C. A.; Leopold, M. C. Evaluating Halogen-Bond Strength as a Function of Molecular Structure Using Nuclear Magnetic Resonance Spectroscopy and Computational Analysis. *J. Phys. Chem. A* **2021**, *125*, 9377−9393.
(44) Sarwar, M. G.; Dragisic, B.; Salsberg, L. J.; Gouliaras, C.; Taylor, M. S. Thermodynamics of Halogen Bonding in Solution: Substituent, Structural, and Solvent Effects. *J. Am. Chem. Soc.* **2010**, *132*, 1646−1653.
(45) Weis, J. G.; Ravnsbæk, J. B.; Mirica, K. A.; Swager, T. M. Employing Halogen Bonding Interactions in Chemiresistive Gas Sensors. *ACS Sens.* **2016**, *1*, 115−119.
(46) Frazier, K. M.; Swager, T. M. Robust Cyclohexanone Selective Chemiresistors Based on Single-Walled Carbon Nanotubes. *Anal. Chem.* **2013**, *85*, 7154−7158.
(47) Johnson, Z. T.; Williams, K.; Chen, B.; Sheets, R.; Jared, N.; Li, J.; Smith, E. A.; Claussen, J. C. Electrochemical Sensing of Neonicotinoids Using Laser-Induced Graphene. *ACS Sens.* **2021**, *6*, 3063−3071.
(48) Duan, H.; Zhang, W.; Zhao, J.; Liang, D.; Yang, X.; Jin, S. A novel halogen bond and a better-known hydrogen bond cooperation of neonicotinoid and insect nicotinic acetylcholine receptor recognition. *J. Mol. Model.* **2012**, *18*, 3867−3875.
(49) Tylkowski, B.; Costa, P. J. The halogen bond: Nature and applications. *Phys. Sci. Rev.* **2017**, *2*, 1.
(50) Dreaden, E. C.; Alkilany, A. M.; Huang, X.; Murphy, C. J.; El-Sayed, M. A. The golden age: gold nanoparticles for biomedicine. *Chem. Soc. Rev.* **2012**, *41*, 2740−2779.
(51) Wayu, M. B.; Pannell, M. J.; Labban, N.; Case, W. S.; Pollock, J. A.; Leopold, M. C. Functionalized carbon nanotube adsorption interfaces for electron transfer studies of galactose oxidase. *Bioelectrochemistry* **2019**, *125*, 116−126.
(52) Frisch, M. J.; Trucks, G. W.; Schlegel, H. B.; Scuseria, G. E.; Robb, M. A.; Cheeseman, J. R.; Scalmani, G.; Barone, V.; Petersson, G. A.; Nakatsuji, H. *Gaussian 16*; Gaussian Inc.: Wallington, CT, 2016.
(53) Zhao, Y.; Truhlar, D. G. The M06 suite of density functionals for main group thermochemistry, thermochemical kinetics, noncovalent interactions, excited states, and transition elements: two new functionals and systematic testing of four M06-class functionals and 12 other functionals. *Theor. Chem. Acc.* **2008**, *120*, 215−241.
(54) Dunning, T. H. Gaussian-Basis Sets for Use in Correlated Molecular Calculations .1. The Atoms Boron through Neon and Hydrogen. *J. Chem. Phys.* **1989**, *90*, 1007−1023.
(55) Kendall, R. A.; Dunning, R. J. Electron affinities of the first-row atoms revisited. Systematic basis sets and wave functions. *J. Chem. Phys.* **1992**, *96*, 6796−6806.
(56) Donald, K. J.; Wittmaack, B. K.; Crigger, C. Tuning sigma-Holes: Charge Redistribution in the Heavy (Group 14) Analogues of Simple and Mixed Halomethanes Can Impose Strong Propensities for Halogen Bonding. *J. Phys. Chem. A* **2010**, *114*, 7213−7222.
(57) Donald, K. J.; Tawfik, M. The Weak Helps the Strong: Sigma-Holes and the Stability of MF4 center dot Base Complexes. *J. Phys. Chem. A* **2013**, *117*, 14176−14183.
(58) Dennington, R.; Keith, T. A.; Millam, J. M. *GaussView*; Semichem Inc.: Shawnee Mission, KS, 2016.
(59) Thordarson, P. Determining association constants from titration experiments in supramolecular chemistry (vol 40, pg 1305, 2011). *Chem. Soc. Rev.* **2011**, *40*, 5922−5923.
(60) Cabot, R.; Hunter, C. A. Non-covalent interactions between iodo-perfluorocarbons and hydrogen bond acceptors. *Chem. Commun.* **2009**, *15*, 2005−2007.
(61) Robertson, C. C.; Wright, J. S.; Carrington, E. J.; Perutz, R. N.; Hunter, C. A.; Brammer, L. Hydrogen bonding vs. halogen bonding: the solvent decides. *Chem. Sci.* **2017**, *8*, 5392−5398.
(62) Libri, S.; Jasim, N. A.; Perutz, R. N.; Brammer, L. Metal fluorides form strong hydrogen bonds and halogen bonds: Measuring interaction enthalpies and entropies in solution. *J. Am. Chem. Soc.* **2008**, *130*, 7842−7844.
(63) Biot, N.; Bonifazi, D. Concurring Chalcogen- and Halogen-Bonding Interactions in Supramolecular Polymers for Crystal Engineering Applications. *Chem.—Eur. J.* **2020**, *26*, 2904−2913.
(64) Hosoya, Y.; Kobayashi, I.; Mizoguchi, K.; Nakada, M. Palladium-Catalyzed Carbothiolation via Trapping of the σ-Alkyl Palladium Intermediate with RSTIPS. *Org. Lett.* **2019**, *21*, 8280−8284.
(65) Kunkle, T.; Abdeen, S.; Salim, N.; Ray, A.-M.; Stevens, M.; Ambrose, A. J.; Victorino, J.; Park, Y.; Hoang, Q. Q.; Chapman, E.; Johnson, S. M. Hydroxybiphenylamide GroEL/ES Inhibitors Are Potent Antibacterials against Planktonic and Biofilm Forms of Staphylococcus aureus. *J. Med. Chem.* **2018**, *61*, 10651−10664.
(66) Brust, M.; Walker, M.; Bethell, D.; Schiffrin, D. J.; Whyman, R. Synthesis of thiol-derivatised gold nanoparticles in a two-phase Liquid−Liquid system. *J. Chem. Soc., Chem. Commun.* **1994**, 801.
(67) Hostetler, M. J.; Wingate, J. E.; Zhong, C.-J.; Harris, J. E.; Vachet, R. W.; Clark, M. R.; Londono, J. D.; Green, S. J.; Stokes, J. J.; Wignall, G. D.; Glish, G. L.; Porter, M. D.; Evans, N. D.; Murray, R. W. Alkanethiolate Gold Cluster Molecules with Core Diameters from 1.5 to 5.2 nm: Core and Monolayer Properties as a Function of Core Size. *Langmuir* **1998**, *14*, 17−30.
(68) Hostetler, M. J.; Templeton, A. C.; Murray, R. W. Dynamics of place-exchange reactions on monolayer-protected gold cluster molecules. *Langmuir* **1999**, *15*, 3782−3789.
(69) Sakthivel, N. A.; Jupally, V. R.; Eswaramoorthy, S. K.; Wijesinghe, K. H.; Nimmala, P. R.; Kumara, C.; Rambukwella, M.; Jones, T.; Dass, A. Size Exclusion Chromatography: An Indispensable Tool for the Isolation of Monodisperse Gold Nanomolecules. *Anal. Chem.* **2021**, *93*, 3987−3996.
(70) Templeton, A. C.; Wuelfing, W. P.; Murray, R. W. Monolayer-Protected Cluster Molecules. *Acc. Chem. Res.* **2000**, *33*, 27−36.
(71) Vargo, M. L.; Gulka, C. P.; Gerig, J. K.; Manieri, C. M.; Dattelbaum, J. D.; Marks, C. B.; Lawrence, N. T.; Trawick, M. L.; Leopold, M. C. Distance Dependence of Electron Transfer Kinetics for Azurin Protein Adsorbed to Monolayer Protected Nanoparticle Film Assemblies. *Langmuir* **2010**, *26*, 560−569.
(72) Ciancaleoni, G. Characterization of Halogen Bonded Adducts in Solution by Advanced NMR Techniques. *Magnetochemistry* **2017**, *3*, 30.
(73) Ciancaleoni, G.; Bertani, R.; Rocchigiani, L.; Sgarbossa, P.; Zuccaccia, C.; Macchioni, A. Discriminating Halogen-Bonding from Other Noncovalent Interactions by a Combined NOE NMR/DFT Approach. *Chem.−Eur. J.* **2015**, *21*, 440−447.
(74) Ingram, R. S.; Hostetler, M. J.; Murray, R. W. Poly-hetero-omega-functionalized alkanethiolate-stabilized gold cluster compounds. *J. Am. Chem. Soc.* **1997**, *119*, 9175−9178.

https://doi.org/10.1021/acs.langmuir.2c00381
Langmuir XXXX, XXX, XXX−XXX

(75) Leopold, M. C.; Doan, T. T.; Mullaney, M. J.; Loftus, A. F.; Kidd, C. M. Electrochemical characterization of self-assembled monolayers on gold substrates derived from thermal decomposition of monolayer-protected cluster films. *J. Appl. Electrochem.* **2015**, *45*, 1069−1084.
(76) Finklea, H. O. Electrochemistry of organized monolayers of thiols and related molecules on electrodes. *Electroanal. Chem.* **1996**, *19*, 110−337.
(77) Daniel, M.-C.; Astruc, D. Gold Nanoparticles: Assembly, Supramolecular Chemistry, Quantum-Size-Related Properties, and Applications toward Biology, Catalysis, and Nanotechnology. *Chem. Rev.* **2004**, *104*, 293−346.
(78) Leopold, M. C.; Donkers, R. L.; Georganopoulou, D.; Fisher, M.; Zamborini, F. P.; Murray, R. W. Growth, conductivity, and vapor response properties of metal ion-carboxylate linked nanoparticle films. *Faraday Discuss.* **2004**, *125*, 63−76.
(79) Russell, L. E.; Pompano, R. R.; Kittredge, K. W.; Leopold, M. C. Assembled nanoparticle films with crown ether-metal ion ″sandwiches″ as sensing mechanisms for metal ions. *J. Mater. Sci.* **2007**, *42*, 7100−7108.
(80) Canzi, G.; Mrse, A. A.; Kubiak, C. P. Diffusion-Ordered NMR Spectroscopy as a Reliable Alternative to TEM for Determining the Size of Gold Nanoparticles in Organic Solutions. *J. Phys. Chem. C* **2011**, *115*, 7972−7978.
(81) El-Sayed, M.; Dickerson, E.; Huang, X. H.; McKay, M.; Yen, C. W. Some exciting properties of gold nanoparticles with applications in fields ranging from energy to medicine. *Abstracts of Papers of the American Chemical Society*; American Chemical Society, 2011; Vol. *242*.

https://doi.org/10.1021/acs.langmuir.2c00381
Langmuir XXXX, XXX, XXX−XXX